Dynamics of wave–current–surge interactions in Lake Michigan: A model comparison

Miaohua Mao, Meng Xia*

Department of Natural Sciences, University of Maryland Eastern Shore, MD, USA

ARTICLE INFO

ABSTRACT

Wave, storm surge dynamics, and wave–current–surge interactions (WCSI) were investigated by applying a pair of unstructured-grid-based models to Lake Michigan under two strong wind events. The effects of wind field sources, wind drag coefficient bulk formula, and parameterizations of the bottom friction term were explored to understand lake dynamics. Two wave models were calibrated by using alternative wave physics settings under the 2011 northeasterly wind event. Forced by the southwesterly wind event in 2013, the calibrated models using the atmosphere–ocean fully coupled Climate Forecast System Version 2 wind field were further validated. It is found that the northwesterly winds induced 0.57 m setup near the southwestern coast, whereas the southwesterly winds produced 0.28 m setup and –0.43 m setdown near the northern and southwestern coasts, respectively. The WCSI mostly influence waves and storm surge in shallow-water areas near coasts and islands through depth-induced breaking, current-induced frequency shift and refraction, and wave-induced setup/setdown through wave radiation stress. Owing to the adoption of different discretization algorithms and bottom friction formulations, the modeled storm surge and waves exhibit some variation between the paired models. Even though the storm surge difference with and without WCSI is smaller than that between the two WCSI-coupled models, both circulation models adopt WCSI considering their consistent improvement on model accuracy under both wind events. The analysis of water transport indicates that wind speed, direction, and coastal geometry and bathymetry are also important factors in storm surge.

© 2016 Elsevier Ltd. All rights reserved.

1. Introduction

Storm winds generate large waves, high surges, and strong currents (Kerr et al., 2013a,b), which further create complex wave–current–surge interactions (WCSI) in the extremely dynamic and shallow regions (Benetazzo et al., 2013; Xie et al., 2008). Longuet-Higgins and Stewart (1964) established the WCSI theory by introducing the concept of two-dimensional (2D) depth-averaged wave radiation stress (WRS) to account for wave-induced setup and setdown. Based on the conservation of wave energy flux, wave height and its steepness become greater when they propagate into shallower regions. The shallow-water wave process is dominated by depth-induced breaking; the momentum flux is then transferred to the water column and raises the water levels adjacent to the coast (Holthuijsen, 2007). Based on the wave–current observations near the southern coast of the North Sea, Wolf and Prandle (1999) proposed that wave propagation and dissipation processes are also affected by variations in local water depth and ambient current

velocity. The analytical solution to account for the effect of currents on waves in the absence of the breaking process was given by Phillips (1977): $\frac{A}{A_0} = \frac{c_0}{\sqrt{c(c+2U)}}$, where A, c, and U are the wave amplitude, phase speed, and ambient current velocity, respectively; A_0 and c_0 refer to the wave amplitude and phase speed without the inclusion of ambient currents. The modification of wave frequency by current is achieved through the Doppler shift effect kU_n, where k is the wave number, and U_n is the current component in the wave direction. This formula relates the absolute frequency ω in a fixed frame of reference with the relative frequency σ in a frame of reference moving with the current through the expression of $\omega = \sigma + kU_n$. From sites A to B, the variations of wave directions (θ_A and θ_B) and wavenumbers (k_A and k_B) on a spatially varying current field are determined by Snell's law, which is expressed as $k_A \sin(\theta_A) = k_B \sin(\theta_B)$ (Holthuijsen, 2007; Longuet-Higgins and Stewart, 1964; Wolf and Prandle, 1999). On the basis of linear wave theory, Mellor (2008) derived the depth-dependable WRS formulation, which further elucidates the underlying physics of WCSI in a three-dimensional (3D) space.

Previous works have laid the foundation of WCSI theory and stimulated intensive numerical studies of wave, storm surge dy-

* Corresponding author.
    E-mail address: mxia@umes.edu (M. Xia).

namics, and complex WCSI process. With the inclusion of wave effects in a circulation model, Xie et al. (2008) made a significant improvement on simulating the surge peak in Charleston Harbor, South Carolina, during the passage of Hurricane Hugo (1989). Liu and Xie (2009) further pointed out that the increase (decrease) of significant wave height (SWH) is highly dependent on the positive (negative) variation of water depth caused by storm surge in shallow-water regions. Using the surge–wave–tide coupled model, Kim et al. (2010) demonstrated that wave-induced setup accounted for 40% of the magnitude of the total surge height in close proximity to the open coast of Tosa Bay, Japan, during Typhoon Anita (1970). Relative to the studies of wave effects on storm surge, significant effects of storm surge on waves in shallow-water regions are less frequently investigated and require further research (Osuna and Monbaliu, 2004). More recently, Olabarrieta et al. (2011) identified wave-induced setup as the primarily factor in the significant wave effect on circulation in the inner part of the Willapa Bay, Washington, during a storm event in October 1998. By applying a Coupled–Ocean–Atmosphere–Wave–Sediment Transport (COAWST) modeling system to the U.S. East Coast and the Gulf of Mexico, Warner et al. (2010) determined that surface waves were highly sensitive to the oceanic and atmospheric coupling processes that occurred during Hurricane Isabel (2003). Subsequently, Benetazzo et al. (2013) applied the COAWST system to the shallow Gulf of Venice during 2011 Bora and Sirocco events, which are fetch-limited northeasterly and long-fetch southeasterly winds, respectively. These works demonstrated that the modeled SWH was substantially enhanced (reduced) due to the inclusion of opposite (unidirectional) currents. Because of coarse grid resolution in resolving the complex coastline and islands and the numerical or physical error introduced by intra-model interpolation along nested boundaries, previous structured-grid-based circulation models using the nesting technique (e.g., Benetazzo et al., 2013; Kim et al., 2010; Liu and Xie, 2009; Osuna and Monbaliu, 2004; Xie et al., 2008) may have inaccuracies (Dietrich et al., 2011; Zijlema, 2010).

The recent emergence of unstructured methods, however, provides an opportunity to better resolve the complex bathymetry and highly irregular coastline and islands in shallow-water regions, which enhances the computational accuracy and efficiency (Dietrich et al., 2011). Such methods have triggered the development of various unstructured-grid-based models, including MIKE3+MIKE21 SW (MIKE3/21 SW; Bolaños et al., 2014), Advanced Circulation Model+Simulating Waves Nearshore (ADCIRC/SWAN; Bunya et al., 2010; Dietrich et al., 2010, 2011, 2012), and Finite Volume Coastal Ocean Model+Surface Wave Model (FVCOM/SWAVE; Chen et al., 2003; Qi et al., 2009; Sun et al., 2013; Wu et al., 2011). Inclusion of WCSI in the modeling system enables computation of the wave action spectral balance equation in the wave model with the inclusion of water surface elevation (WSE) and current velocity fields and simultaneously passes the 2D/3D WRS gradients back to the circulation model to account for momentum flux. Chen et al. (2013) reported that the WCSI intensity was relatively appreciable inside Scituate Harbor, Massachusetts, during the 2007 Patriot's Day Storm. They further attributed the difference in modeled SWH and WSE between ADCIRC/SWAN and FVCOM/SWAVE to the application of different discretization algorithms and bottom friction formulations. With the inclusion of WCSI, the FVCOM circulation model reduced the underestimation of the 0.9 m high storm surge from 23 cm to 15 cm during the December 2010 nor'easter event in Scituate (Beardsley et al., 2013).

Although WCSI was successfully tested by model-to-model comparisons (Chen et al., 2013), direct evaluation of the unstructured-grid-based model's performance using field observations has been barely reported. By using adequate data collected during Hurricanes Ike (2008) and Rita (2005) in the Gulf of Mexico,

Kerr et al. (2013b) determined that although both circulation-only and wave-only models satisfactorily reproduced storm surge and surface waves, respectively, the two-way coupled ADCIRC/SWAN yielded the most accurate results. Given that FVCOM and SWAN are one-way offline coupled, however, a direct comparison of fully and dynamically coupled modeling systems is still lacking. Most importantly, no consensus has been reached regarding the intensity of WCSI, which was shown to be relatively strong in the shallow Harbor and weak in the deep Gulf. Therefore, it would be worthwhile to explore the significance of WCSI with additional numerical applications and model calibration and validation. Considering the dominant role of wind forcing both in circulation and wave dynamics in a semi-enclosed basin (Benetazzo et al., 2013), sensitivity tests to explore the key factors influencing surface wind stress, including various wind field sources and wind drag coefficients, are likely important. By using the wind field derived from alternative data sources (e.g., the Global Environmental Multiscale (GEM) and North American Mesoscale models) in ADCIRC, Chittibabu and Rao (2012) detected different spatiotemporal patterns of WSE and storm surge in Lake Winnipeg, Canada, during the October 2010 storm. For the Great Lakes system, Jensen et al. (2012) hindcasted seven storms passing over Lake Michigan in 1989–2009. By replacing the observation-based Natural Neighbor Method (NNM) winds with the atmospheric modeled data from the Climate Forecast System Reanalysis (CFSR), a higher skill level in storm surge simulation was achieved. Based on the storm surge simulation of an Ivan-like storm in Tampa Bay, Florida, Weisberg and Zheng (2008) illustrated that surge height is positively related to surface wind stress according to the wind drag coefficient bulk formula.

In this study, we configured a pair of coupled modeling systems to simulate storm surge, wave dynamics, and WCSI processes in Lake Michigan. Overall, three main questions are addressed: (1) How sensitive is the storm surge simulation in response to various wind forcing and wind drag coefficient bulk formulae? (2) How do storm surge and waves develop under strong wind conditions in Lake Michigan? (3) How will the simulations differ by using alternative WCSI-coupled modeling systems and those with and without WCSI? The remaining sections of this study are organized as follows. The following section introduces the methodology, which includes descriptions of the study domain and model meshes, coupling system, data sources, numerical experiments, and skill metrics. Sensitivity and calibration results are described and analyzed in Section 3, followed by a validation experiment in Section 4. In Section 5, numerical results addressing the aforementioned question (3) are reported, and dynamic responses of the depth-integrated water transport flux (DWTF) to the synergistic effect of wind forcing and coastal bathymetry and geometry are discussed. A summary and conclusions are given in Section 6.

2. Methodology

2.1. Study domain and model meshes

Lake Michigan is the third largest lake in the Great Lakes system by surface area (58,000 km²). At about 494 km long and 190 km wide, the elongated semi-enclosed basin is delimited by land boundaries on three sides and conjoins at the northeastern corner with Lake Huron via the Straits of Mackinac at a mean depth of ~20 m (Fig. 1a and b). From north to south, the smooth and deep mid-lake area includes the Chippewa Basin, Mid-Lake Plateau, and South Chippewa Basin. Two island chains, Beaver Island and North Manitou Island, and two bays, the shallow and elongated Green Bay and the deep Grand Traverse Bay, are located in the middle and on the flanks of the Chippewa Basin, respectively. Green Bay and Grand Traverse Bay meet Lake Michi-
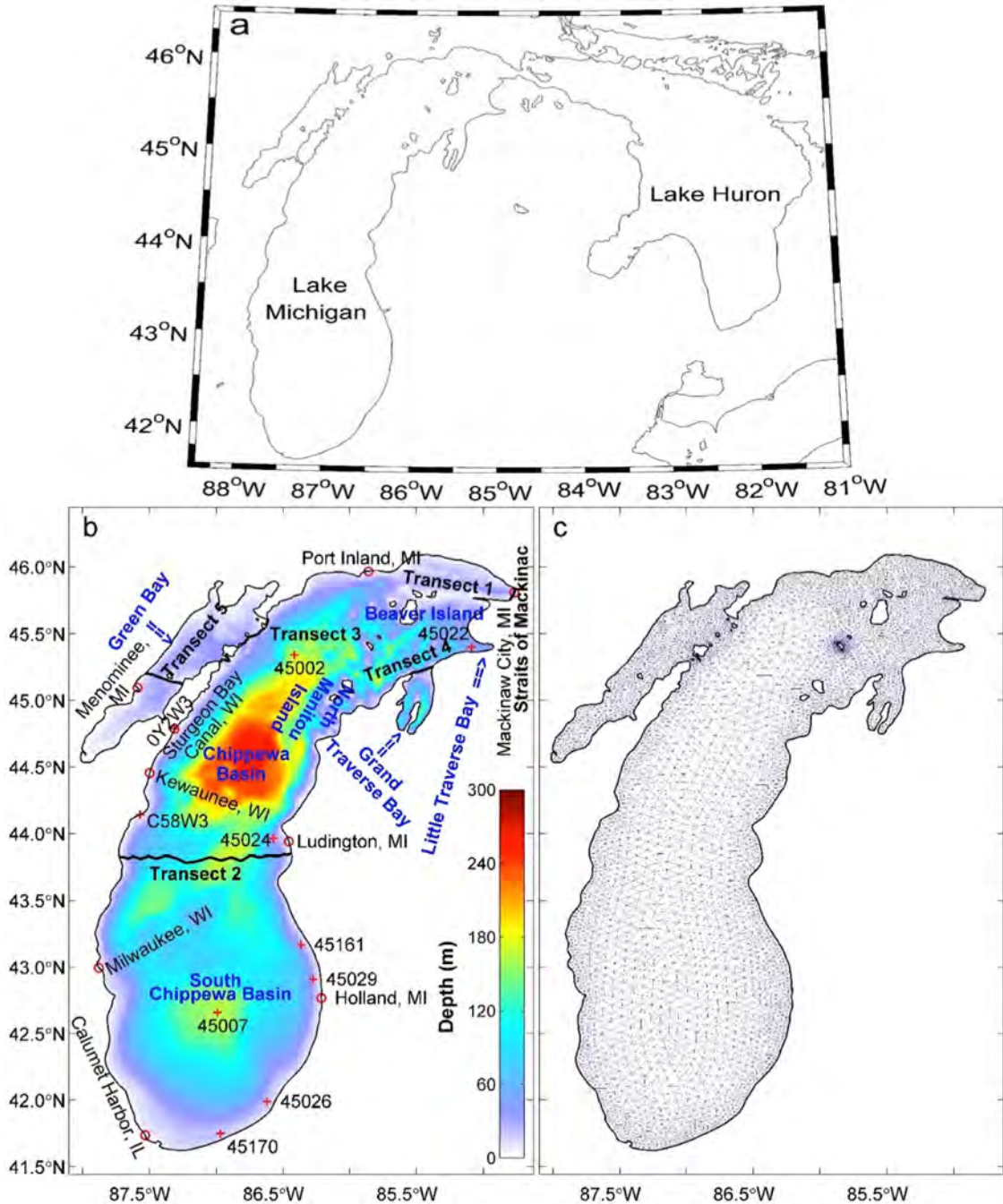
Fig. 1. (a) Maps of Lakes Michigan and Huron, (b) bathymetry and locations of the NOS gauges (red open circles) and NDBC buoys (red plus signs) and (c) computational meshes for Lake Michigan. Transects 1–5 were selected to study the DWTF for lake–lake, basin–basin, basin–bay (Lake Michigan–Green Bay and Lake Michigan–Grand Traverse Bay), and area–area (lower and upper Green Bay), respectively. (For interpretation of the references to color in this figure legend, the reader is referred to the web version of this article.)

gan through eastwardly and northwardly orientated inlet mouths, respectively. Medium-resolution unstructured meshes with 5256 nodes and 9581 elements (relative to the high-resolution version discussed in Mao et al., 2016) were adopted in the WCSI-coupled modeling system (Fig. 1c). The mesh size of the unstructured grids, varied from ~340 m near the coast and islands to 7.6 km in the mid-lake area. In particular, fine resolution was applied in the shallow-water regions to resolve the highly steep bathymetry and irregular coastline and islands. A modeling system with unstructured meshes represents the multi-scale lake dynamics properly and shows high computational efficiency.

2.2. WCSI-coupled modeling system

In this study, WCSI-coupled modeling systems explain the wave-induced setup and alongshore currents by using the concept of 2D WRS gradients. A two-way coupling process is achieved through the transfer of WSE and depth-averaged current velocity fields from the circulation model to the wave model and by the passing of 2D WRS from the wave model back to the circulation model synchronously. In addition to using the 2D WRS to account for the wave effects, other processes include wave-induced sea surface roughness (Donelan et al., 1993) and bottom stress

(Liu and Xie, 2009), turbulence and momentum flux during wave breaking, and Stokes drift (Röhrs et al., 2012). An alternative mechanism representing the wave effects on currents is based on the concept of vortex force (VF). The VF-based formulation was originally derived by Craik and Leibovich (1976) to consider wave-averaged forcing on currents. The analytical solution used to estimate the effects of mean wave momentum on current vorticity was proposed by McWilliams et al. (2004). The VF-based approach elucidated Langmuir circulations through current-generated wave vorticity and the vortex stretching by Stokes drift (Lane et al., 2007), which was subsequently implemented in the COAWST modeling system by Kumar et al. (2012). For this study, however, we focused on the dynamic comparison of 2D ADCIRC/SWAN and FVCOM/SWAVE WRS-based coupling systems. Detailed descriptions of both modeling systems are given below.

2.2.1. Descriptions of ADCIRC/SWAN

This study applied the 2D depth-integrated explicit barotropic circulation model ADCIRC-2DDI, hereafter referred to as ADICRC for brevity (Luettich and Westrink, 2004), in the ADCIRC/SWAN modeling system (Dietrich et al., 2010). The 2D shallow water equations in ADCIRC were discretized by using a continuous-Galerkin finite-element method (FEM) and finite-difference method (FDM) in the geographic space and for the time-stepping scheme, respectively (Dawson et al., 2006). When coupled with a wave model, ADCIRC computes the eddy viscosity with enhanced mixing due to a wave-breaking event in the MY-2.5 turbulence closure model. A constant production parameter (i.e., 150) was used to calculate the wave-induced turbulence kinetic energy (TKE) flux and sea surface roughness. Additionally, the wave–current coupled model includes both wave-induced and current-induced bottom friction stress (Dietrich et al., 2011). The WSE and depth-averaged current velocity fields were computed in the Generalized Wave-Continuity Equation and 2DDI momentum equation, respectively. The computational time step was set at 4 s. The bottom stress was computed by using the quadratic bottom friction law, mathematically expressed as:

$$\left(\tau_{bx}, \tau_{by}\right) = \rho C_d (\bar{u}, \bar{v})\sqrt{\bar{u}^2 + \bar{v}^2}, \tag{1}$$

where (τ_{bx}, τ_{by}) and $(\bar{u}, \bar{v})$ are the bottom stress and depth-averaged current velocity in the (x, y) plane respectively, and C_d denotes bottom drag coefficient.

The air–sea momentum flux is transferred through the surface wind stress $\tau = \rho_{air}C_DU_{10}^2$, where ρ_{air}, C_D, and U_{10} are the air density, wind drag coefficient, and wind speed at 10 m elevation, respectively. The wind drag coefficient bulk formula proposed by Garratt (1977), hereafter referred to as G77, is incorporated into the default ADCIRC:

$$C_D = (0.75 + 0.067U_{10}) \times 10^{-3}. \tag{2}$$

The wave model adopted in the ADCIRC/SWAN modeling system is the unstructured-grid version of the third-generation wind-wave model SWAN (Zijlema, 2010). It computes the wave generation, propagation, transfer, and dissipation processes based on the wave action density spectrum balance equation (Booij et al., 1999; Zijlema, 2010):

$$\frac{\partial N}{\partial t} + \frac{\partial (C_{g,x} + U_x)N}{\partial x} + \frac{\partial (C_{g,y} + U_y)N}{\partial y} + \frac{\partial C_{g,\sigma}N}{\partial \sigma} + \frac{\partial C_{g,\theta}N}{\partial \theta} = \frac{S_{tot}}{\sigma}, \tag{3}$$

where σ is the intrinsic frequency, θ is the wave direction taken counterclockwise from the geographic east, N denotes the wave action spectral density, t is time, and C_g is the wave group velocity in space $(x, y, \sigma, \text{ and } \theta)$. The left-hand side of Eq. (3) represents the changes in wave action density in time and geographic space and

those owing to the depth-induced and current-induced frequency shift and refraction, respectively; the current is depth-averaged in the 2D model. The wave energy sources and sinks S_{tot} include the wave growth generated by wind input, nonlinear transfer of wave energy through three-wave and four-wave interactions, wave decay owing to whitecapping and bottom friction, and depth-induced breaking.

The governing Eq. (3) was discretized with a vertex-based, first-order, backward-space, backward-time scheme and a hybrid central or upwind scheme in the wave spectral space. This implicit geographical propagation scheme avoids the strict Courant-Friedrichs-Lewy (CFL) limitation on the time step; however, a CFL value of 0.5 in the directional space was used to restrict excessive depth-induced refraction over the region with under-resolved bathymetry. The wave directions were evenly split into 36 bins with a constant bandwidth of 10°, and wave frequencies were discretized over 32 bins that increased logarithmically from 0.0512 Hz to 1 Hz. The time step of 5 min used in SWAN is equivalent to that for the coupling process.

2.2.2. Descriptions of FVCOM/SWAVE

The FVCOM circulation model in the FVCOM/SWAVE modeling system (Wu et al., 2011) was developed and upgraded by Chen et al. (2003, 2008, 2011). This model solves the primitive equations by adopting a second-order upwind finite-volume method (FVM) and a modified explicit fourth-order Runge–Kutta time-stepping scheme for the advection and time integration, respectively. The mode-split technique is realized by advancing the external and internal modes at 4 and 16 s, respectively. The continuity and momentum equations are closed up by the MY-2.5 scheme and eddy parameterization for the vertical (Galperin et al., 1988; Mellor and Yamada, 1982) and horizontal mixing (Smagorinsky, 1963), respectively. Recently, Mellor and Blumberg (2004) introduced the wave effects on TKE flux through the surface boundary into the MY-2.5 model, i.e., the dependence of TKE production parameter on wave age. Detailed descriptions and comparisons of various second-order two-equation turbulence closure models (e.g., k-ε, k-ω, and k-gen) have been reported by Carniel et al. (2009). The preliminary configuration of 3D FVCOM consists of three terrain-following sigma layers in the vertical coordinate system. The bottom friction stress is calculated from a quadratic expression:

$$\left(\tau_{bx}, \tau_{by}\right) = \rho C_d(u_b, v_b)\sqrt{u_b^2 + v_b^2}, \tag{4}$$

where (u_b, v_b) denotes the bottom current velocities in space (x, y); the bottom drag coefficient C_d is determined by matching the logarithmic bottom layer at a height of z_{zb} above the bottom, which is expressed as

$$C_d = \max\left[\frac{\kappa^2}{ln\left(\frac{z_{zb}}{z_0}\right)^2}, 0.0025\right], \tag{5}$$

where $\kappa = 0.41$ is the von Karman constant, and z_0 is the bottom roughness length.

To compare with the ADCIRC circulation model and to eliminate the bias introduced by the 2D and 3D models, this study adopted the 2D FVCOM model, which uses depth-averaged current velocity to calculate the bottom friction stress in Eq. (4). It should be mentioned that the depth-averaged and depth-dependent current velocity is passed to the wave model in the 2D and 3D coupled FVCOM/SWAVE, respectively. Theoretical derivation and detailed comparison of the 2D and 3D models (e.g., WRS formulations and Stokes drift) have been reported by Longuet-Higgins and Stewart (1964), Mellor (2008), and Sheng and Liu (2011). Enhanced bottom roughness length and bottom friction stress owing to the presence of waves (e.g., bottom wave orbital velocity) in FVCOM are based

on the wave–current bottom boundary theory proposed by Madsen (1994).

The default bulk formula (Large and Pond, 1981), hereafter referred to as LP81, for wind drag coefficient adopted by FVCOM is expressed as

$$C_D = \begin{cases} 1.2 \times 10^{-3} & U_{10} < 11 \text{ m/s} \\ (0.49 + 0.065 \times U_{10}) \times 10^{-3} & 11 \text{ m/s} \leq U_{10} \leq 25 \text{ m/s} \\ 2.115 \times 10^{-3} & U_{10} > 25 \text{ m/s} \end{cases} \tag{6}$$

Because the maximum wind speed at 10 m elevation U_{10} in Lake Michigan, at 21.9 m/s, is below the cutoff value of $\sim$33 m/s suggested by Powell et al. (2003), no upper limit was applied to restrict the wind drag coefficient in both modeling systems. The contribution of waves to the enhanced wind stress (e.g., sea surface roughness) is a function of wave age (Donelan et al., 1993).

For the 3D baroclinic FVCOM, the net surface heat flux ($HFLX$) is calculated by using atmospheric variables including wind speed, air temperature, lake surface temperature (T_s), relative humidity, and downward shortwave (SW_{down}), downward longwave (LW_{down}), and upward longwave (LW_{up}) radiations. The surface heat flux budget model is expressed as

$$HFLX = SW_{down} + LW_{down} + LW_{up} + H_{sensible} + H_{latent}. \tag{7}$$

The SW_{down} and LW_{down} data were collected from the standard 3-hourly output of the GEM atmospheric model (Côté et al., 1998) and were interpolated to computational cells with hourly intervals. The σ in the upward longwave radiation expression $LW_{up} = -\sigma T_a^4$ represents the Stefan-Boltzmann constant (5.67×10^{-8} W m^{-2} K^{-4}). The sensible ($H_{sensible}$) and latent (H_{latent}) heat transfers were calculated on the basis of the bulk aerodynamic formulation COARE 2.6 developed by Fairall et al. (1996).

The FVM-based wave model SWAVE solves the same governing equation as the FDM-based SWAN with a different discretization algorithm and numerical scheme (Qi et al., 2009). The frequency and directional space in SWAVE is discretized with the Flux-Corrected Transport algorithm and implicit Crank-Nicolson method, respectively. An implicit second-order upwind finite-volume scheme is taken in the geographic space. Wave diffraction is turned off considering computational stability. The wave frequency σ is discretized into 10 bins with a logarithmic increment over the range of 0.04–1 Hz, and the wave direction θ is split into 36 bins with a constant bandwidth of 10°. The time interval for the wave calculation in SWAVE is 16 s, which is equal to the data transfer step in the WCSI-coupled modeling system.

2.3. Model input and observational data

The National Geophysical Data Center's (NGDC) bathymetric data, with 6′ resolution (about 185 m longitudinal and 133 m latitudinal), were interpolated to the computational cells (Fig. 1c). The external atmospheric forcing includes the spatiotemporally varying wind speed and air pressure fields. The three wind field sources included: (a) the Great Lakes Environmental Research Laboratory's (GLERL) NNM-based (Schwab and Morton, 1984) hourly, 2 km-resolution forcing, which was interpolated from lake buoys at mid-lake stations 45,002 and 45,007 and from several nearshore stations and coastal land sites (Lang and Leshkevich, 2014); (b) the Canadian Meteorological Center's (CMC) 3-hourly, 10 km-resolution forcing produced from the GEM model, assimilating both in situ and remotely sensed satellite data (Côté et al., 1998); and (c) the National Centers for Environmental Prediction's Climate Forecast System Version 2 (CFSv2) hourly, $\sim$23 km-resolution reanalyzed data, which assimilate data from surface, upper balloon, aircraft, and satellite observations (Saha et al., 2014). The CFSv2 wind

data are produced from a two-way atmosphere–ocean fully coupled modeling approach, whereas the GEM or NNM data are produced from one-way atmospheric models or are interpolated from observations of scattered buoys and meteorological stations without considering the two-way air–sea interactions. The air pressure data retrieved from the GEM model was adopted for all simulations. Hourly WSEs collected from the National Ocean Service (NOS) across the Straits of Mackinac in Mackinaw City, Michigan, and around the lake's perimeter (Fig. 1a and b) were processed and used for open boundary conditions and model calibration/validation, respectively. Data from the buoys positioned in the mid-lake area and along the coast (Fig. 1b) were retrieved from the National Data Buoy Center (NDBC) and include hourly wind speed, SWH, peak wave period (PWP), and mean wave direction (MWD). Details of the locations and water depths of the NOS gauges and NDBC buoys are presented in Table 1. River discharges into the lake were not included because their effects on storm surge and wave dynamics were assumed to be limited.

2.4. Design of numerical experiments

The storm surge and wave simulations were conducted during two strong but distinct wind events that were dominated by northeasterly winds on October 14–24, 2011, and southwesterly winds on October 24–28, 2013, respectively. In the 2011 wind event, the sensitivity of storm surge in response to various wind field sources and different parameterizations for the wind drag coefficient bulk formula was examined, followed by calibration experiments for the wave models using various wave physics settings. The calibration of the circulation model for WSE simulation was conducted with different parameterizations for the bottom friction formulation over the period of April–October 2011. The WSE was obtained by subtracting 176 m from the water surface level provided in the International Great Lakes Datum of 1985. The value was initialized to zero about six and two days prior to the surge peaks of the 2011 and 2013 wind events for storm surge simulation, respectively. The calibrated model was further validated by hindcasting the storm surge and wave dynamics for the 2013 wind event. To investigate the effects of WCSI, additional numerical experiments using the WCSI-coupled modeling system were run and analyzed for the 2011 and 2013 wind events. Detailed numerical settings of the designed experiments are listed in Tables 2 and 3. To study the relative importance of wave effects other than the WRS-induced setup/setdown, numerical cases excluding the wave-induced bottom stress and bottom roughness length, sea surface roughness, Stokes drift, and including the momentum and TKE flux during wave breaking were added individually (Cases 3e–3f). The baseline model for these additional numerical tests is the validated WCSI-coupled 2D barotropic FVCOM/SWAVE (Case 3d).

The 2D circulation models, ADCIRC and FVCOM, were spun up for one month before outputting the WSE simulations over the period of April–October 2011 for model calibration. For the October 14–24, 2011, wind event, the barotropic circulation models and wave models, ADCIRC, FVCOM, SWAN, and ADCIRC/SWAN, were run from cold starts on September 17; SWAVE and FVCOM/SWAVE cold starts occurred on September 22. For the October 24–28, 2013, wind event, all of the barotropic circulation models and wave models were spun up with cold starts on October 15. The initial conditions for the 3D baroclinic FVCOM/SWAVE model were spatially uniform water temperature at 4 °C and zero salinity and current velocity on April 1 for both the 2011 and 2013 wind events. The calculated 3D hydrodynamic and wave fields were used as hot start files to drive the WCSI-coupled 3D baroclinic model on September 22 and October 15 for the 2011 and 2013 wind events, respectively.

To examine the synergistic effects of atmospheric winds and coastal bathymetry and geometry on storm surge (e.g., potential in-

Table 1
Locations and water depths for the NOS's WSE gauges and NDBC buoys in Lake Michigan.

Observational station		Observed variable	Data source	Long. (°)	Lat. (°)	Depth (m)
1	Calumet Harbor, IL	WSE	NOS	–87.538	41.730	3.8
2	Ludington, MI	WSE	NOS	–86.442	43.947	6.2
3	Milwaukee, WI	WSE	NOS	–87.887	43.002	4.4
4	Holland, MI	WSE	NOS	–86.202	42.768	8.1
5	Menominee, MI	WSE	NOS	–87.590	45.095	4.8
6	Port Inland, MI	WSE	NOS	–85.872	45.970	6.5
7	Kewaunee, WI	WSE	NOS	–87.502	44.463	4.4
8	Sturgeon Bay Canal, WI	WSE	NOS	–87.313	41.714	3.5
9	Mackinaw City, MI	WSE	NOS	–86.559	43.977	25.0
10	NDBC 45,029	Wave	Limno Tech	–86.272	42.9	30
11	NDBC 45,026	Wave	Limno Tech	–86.617	44.795	5.4
12	NDBC 0Y2W3	Wave	USCG	–87.313	44.794	5.4
13	NDBC C58W3	Wave	USCG	–87.563	44.146	5.9
14	NDBC 45,170	Wave	IISG & PCE	–86.968	41.755	19
15	NDBC 45,161	Wave	GLERL	–86.361	43.178	25
16	NDBC 45,024	Wave	UM-CILER	–86.559	43.977	30.3
17	NDBC 45,022	Wave	MTU	–84.721	45.403	49.1
18	NDBC 45,002	Wave	NDBC	–86.411	45.777	175.3
19	NDBC 45,007	Wave	NDBC	–87.026	42.674	160

Table 2
B for setup and setdown, the *RMSD* and *CC* scores for WSE from the designed numerical experiments for ADCIRC and FVCOM, and the *MAV* and *SDAV* for WSE from observations. BDC and BRL represent the bottom drag coefficient and bottom roughness length, respectively. The numerical Cases 1a–1d and 1f–1g were used for the preliminary assessment of ADCIRC and FVCOM, respectively. Cases 2a–2c and 2d–2e are the calibration experiments for ADCIRC and FVCOM, respectively. Cases 3a and 3c are the validations for ADCIRC and FVCOM, respectively. The effect of WCSI on storm surge was analyzed with the additional WCSI-coupled ADCIRC/SWAN (Cases 1e and 3b) and FVCOM/SWAVE (Cases 1h and 3d).

Case Name	Simulation Period	Model Type	WCSI Effect	Wind Source	Bulk Formula	BDC(BRL)	*RB* for Setup	*RB* for Setdown	*RMSD*	*CC*	*MAV*	*SDAV*
1a	2011 October 14–24	ADCIRC	Off	GEM	G77	0.002	–0.21	/	8.8 cm	0.93	11.2 cm	7.5 cm
1b	2011 October 14–24	ADCIRC	Off	NNM	G77	0.002	–0.33	/	9.3 cm	0.86	11.2 cm	7.5 cm
1c	2011 October 14–24	ADCIRC	Off	CFSv2	G77	0.002	–0.13	/	8.5 cm	0.91	11.2 cm	7.5 cm
1d	2011 October 14–24	ADCIRC	Off	CFSv2	LP81	0.002	–0.26	/	9.0 cm	0.88	11.2 cm	7.5 cm
1e	2011 October 14–24	ADCIRC	On	CFSv2	G77	0.002	–0.06	/	8.5 cm	0.90	11.2 cm	7.5 cm
1f	2011 October 14–24	FVCOM	Off	CFSv2	G77	0.1 cm	–0.01	/	7.1 cm	0.78	11.2 cm	7.5 cm
1g	2011 October 14–24	FVCOM	Off	CFSv2	LP81	0.1 cm	–0.12	/	7.7 cm	0.73	11.2 cm	7.5 cm
1h	2011 October 14–24	FVCOM	On	CFSv2	G77	0.1 cm	0.01	/	6.2 cm	0.84	11.2 cm	7.5 cm
2a	2011 April–October	ADCIRC	Off	CFSv2	G77	0.002	/	/	7.1 cm	0.98	20.1 cm	8.5 cm
2b	2011 April–October	ADCIRC	Off	CFSv2	G77	0.0025	/	/	7.2 cm	0.98	20.1 cm	8.5 cm
2c	2011 April–October	ADCIRC	Off	CFSv2	G77	0.003	/	/	7.2 cm	0.98	20.1 cm	8.5 cm
2d	2011 April–October	FVCOM	Off	CFSv2	G77	0.1 cm	/	/	4.0 cm	0.97	20.1 cm	8.5 cm
2e	2011 April–October	FVCOM	Off	CFSv2	G77	0.5 cm	/	/	4.5 cm	0.96	20.1 cm	8.5 cm
2f	2011 April–October	FVCOM	Off	CFSv2	G77	1.0 cm	/	/	4.4 cm	0.96	20.1 cm	8.5 cm
3a	2013 October 24–28	ADCIRC	Off	CFSv2	G77	0.002	–0.13	0.01	6.7 cm	0.75	6.8 cm	4.7 cm
3b	2013 October 24–28	ADCIRC	On	CFSv2	G77	0.002	–0.10	–0.01	6.6 cm	0.75	6.8 cm	4.7 cm
3c	2013 October 24–28	FVCOM	Off	CFSv2	G77	0.1 cm	–0.26	–0.16	5.8 cm	0.64	6.8 cm	4.7 cm
3d	2013 October 24–28	FVCOM	On	CFSv2	G77	0.1 cm	–0.24	–0.10	5.7 cm	0.75	6.8 cm	4.7 cm

flow from Lake Huron), the DWTFs produced from ADCIRC/SWAN across five typical transects (Fig. 1b) were calculated as expressed below:

$$DWTF = \frac{1}{t_2 - t_1} \sum_{t=t_1}^{t=t_2} \left| \vec{v} \cdot \hat{n} \right| \cdot d \cdot (z+h), \qquad (8)$$

where $\vec{v}$ is the current velocity, $\hat{n}$ is the unit vector normal to the transect, d is the transect width, the water depth $(z+h)$ is the summation of WSE and lake bathymetry, and t_1 and t_2 are the starting and ending times for the calculations. The calculation time for the DWTF is a 6-h period before reaching the surge peaks in the 2011 and 2013 wind events. The DWTF is defined as positive when the

Table 3
Wave physics settings from the designed numerical experiments for SWAN and SWAVE. Cases 4a and 4b–4c are the model calibrations for SWAN and SWAVE, respectively. SWAN (Case 5a) and SWAVE (Case 5c) were validated for the 2013 wind event. The effect of WCSI on wave dynamics was analyzed by using ADCIRC/SWAN (Cases 4d and 5b) and FVCOM/SWAVE (Case 5d).

Case	Simulation period	Model type	WCSI effect	Wind input	Whitecapping dissipation	Depth-induced breaking formulation
4a	2011 October 14–24	SWAN	Off	Janssen (1991)	Readjusted Rogers et al. (2003) with $C_{ds} = 3.0 \times 10^{-5}$ and $\delta = 0.3$	TG83 with $\gamma_{TG} = 0.42$
4b	2011 October 14–24	SWAVE	Off	Snyder et al. (1981)	Komen et al. (1984) with $C_{ds} = 2.36 \times 10^{-5}$ and $\delta = 0$	BJ78 with $\gamma_{BJ} = 0.73$
4c	2011 October 14–24	SWAVE	Off	Janssen (1991)	Readjusted Rogers et al. (2003) with $C_{ds} = 3.0 \times 10^{-5}$ and $\delta = 0.3$	TG83 with $\gamma_{TG} = 0.42$
4d	2011 October 14–24	SWAN	On	Janssen (1991)	Readjusted Rogers et al. (2003) with $C_{ds} = 3.0 \times 10^{-5}$ and $\delta = 0.3$	TG83 with $\gamma_{TG} = 0.42$
5a	2013 October 24–28	SWAN	Off	Janssen (1991)	Readjusted Rogers et al. (2003) with $C_{ds} = 3.0 \times 10^{-5}$ and $\delta = 0.3$	TG83 with $\gamma_{TG} = 0.42$
5b	2013 October 24–28	SWAN	On	Janssen (1991)	Readjusted Rogers et al. (2003) with $C_{ds} = 3.0 \times 10^{-5}$ and $\delta = 0.3$	TG83 with $\gamma_{TG} = 0.42$
5c	2013 October 24–28	SWAVE	Off	Janssen (1991)	Readjusted Rogers et al. (2003) with $C_{ds} = 3.0 \times 10^{-5}$ and $\delta = 0.3$	TG83 with $\gamma_{TG} = 0.42$
5d	2013 October 24–28	SWAVE	On	Janssen (1991)	Readjusted Rogers et al. (2003) with $C_{ds} = 3.0 \times 10^{-5}$ and $\delta = 0.3$	TG83 with $\gamma_{TG} = 0.42$

transports of basin–basin in Lake Michigan and area–area in Green Bay, lake–lake, and basin–bay point toward north, into Lake Michigan, and into Green Bay and Grand Traverse Bay, respectively. To study the influences of deep-water return flows and baroclinic oscillations on the modeled flow patterns, rudimentary simulations from the 3D barotropic and baroclinic FVCOM/SWAVE with three sigma-layers in the 2013 wind event were included.

2.5. Skill metrics

Model performance was assessed on the basis of relative bias (*RB*), root-mean-square deviation (*RMSD*), Pearson correlation coefficient (*CC*), mean of absolute value (*MAV*), and standard deviation of absolute value (*SDAV*), which are expressed as

$$RB = \frac{\sum_{n=1}^{N} (Model_n - Obs_n)}{\sum_{n=1}^{N} |Obs_n|}, \tag{9}$$

$$RMSD = \left[\frac{1}{N} \sum_{n=1}^{N} (Model_n - Obs_n)^2 \right]^{1/2}, \tag{10}$$

$$CC = \frac{\frac{1}{N} \sum_{n=1}^{N} \left(Obs_n - \overline{Obs} \right) \left(Model_n - \overline{Model} \right)}{\sigma_{Model_n} \sigma_{Obs_n}}, \tag{11}$$

$$MAV = \frac{1}{N} \sum_{n=1}^{N} |Obs_n| \tag{12}$$

$$SDAV = \left[\frac{1}{N} \sum_{n=1}^{N} \left(Obs_n - \overline{Obs_n} \right)^2 \right]^{1/2} \tag{13}$$

where $\overline{Obs}$ and $\overline{Model}$ are the averaged values from observation (Obs_n) and model ($Model_n$) in a sample of size *N*, and σ_{Obs_n} and σ_{Model_n} are the corresponding standard deviations. In the 2011 and 2013 wind events, the *RB* for setup was calculated at Calumet Harbor, Illinois, hereafter referred to as CH, and Port Inland, Michigan, hereafter referred to as PI, respectively. The *RB* for setdown was calculated at CH in the 2013 wind event. The ensembles of *RMSD, CC, MAV,* and *SDAV* for WSE and SWH are the averaged results of the individual value computed at the respective NOS gauge and NDBC buoy.

3. Sensitivity analysis and calibration experiments

The Ohio Valley Low storm passed over Lake Michigan on October 20, 2011 (Bardou and Birk, 2012), generating strong winds of 23 m/s and extreme waves of 5.9 m at NDBC station 45,007 (www.ndbc.noaa.gov) and high surge of 0.57 m near the southwestern coast (http://oceanservice.noaa.gov/programs/coops). The sensitivity of storm surge in response to various wind field sources and alternative wind drag coefficient bulk formulae are shown here. Subsequently, the model calibrations on the parameterizations of the bottom friction term and wave physics settings are presented.

3.1. Sensitivity to various wind field sources

Fig. 2 shows the time series of WSE covering the surge peaks produced from ADCIRC forced by GEM, NNM, and CFSv2 wind fields (Cases 1a–1c) versus observed values at eight NOS gauges recorded October 14–24, 2011. The statistical scores for storm surge (e.g., *RB*) and WSE (e.g., *RMSD, CC, MAV*, and *SDAV*) are presented in Table 2, which shows the largest *RMSD* score below 9.3 cm and the smallest *CC* score at more than 0.86. On average, all three simulations reproduced the temporal variations of WSE satisfactorily. Owing to a slight difference in wind source, ADCIRC yielded different simulations for the surge peak. The time series of wind speed and direction produced from the GEM, NNM, and CFSv2 fields were compared with NDBC buoy observations for the 2011 wind event (Fig. 3a and b). The estimated peaks of wind speed at CH were 17.5, 13.6 and 16.5 m/s from the CFSv2, GEM and NNM fields, respectively, and the wind direction from the GEM model pointed toward the large, concave, southwestern coast in a more perpendicular direction than that from the NNM data. Consequently, the smallest underestimation of 13% for the observed surge peak at CH, at 0.57 m height, was produced from the CFSv2 winds; this value increased to 21% and 33% from the GEM and NNM winds (Table 2). In addition, the predictions for the arrival time of the surge peak (07:00 GMT on October 20) from the CFSv2, GEM, and NNM winds preceded the observation by 1h, 2h, and 3h, respectively. Therefore, the model driven by the CFSv2 wind forcing performed better in reproducing the storm surge despite its low spatial resolution. The physical explanation should be related to the fact that its spatial wind field was derived from the two-way atmosphere–ocean fully coupled modeling approach (Saha et al., 2014); the GEM data were produced from the one-way atmosphere–ocean coupling process (Côté et al., 1998), and the NNM data were interpolated from
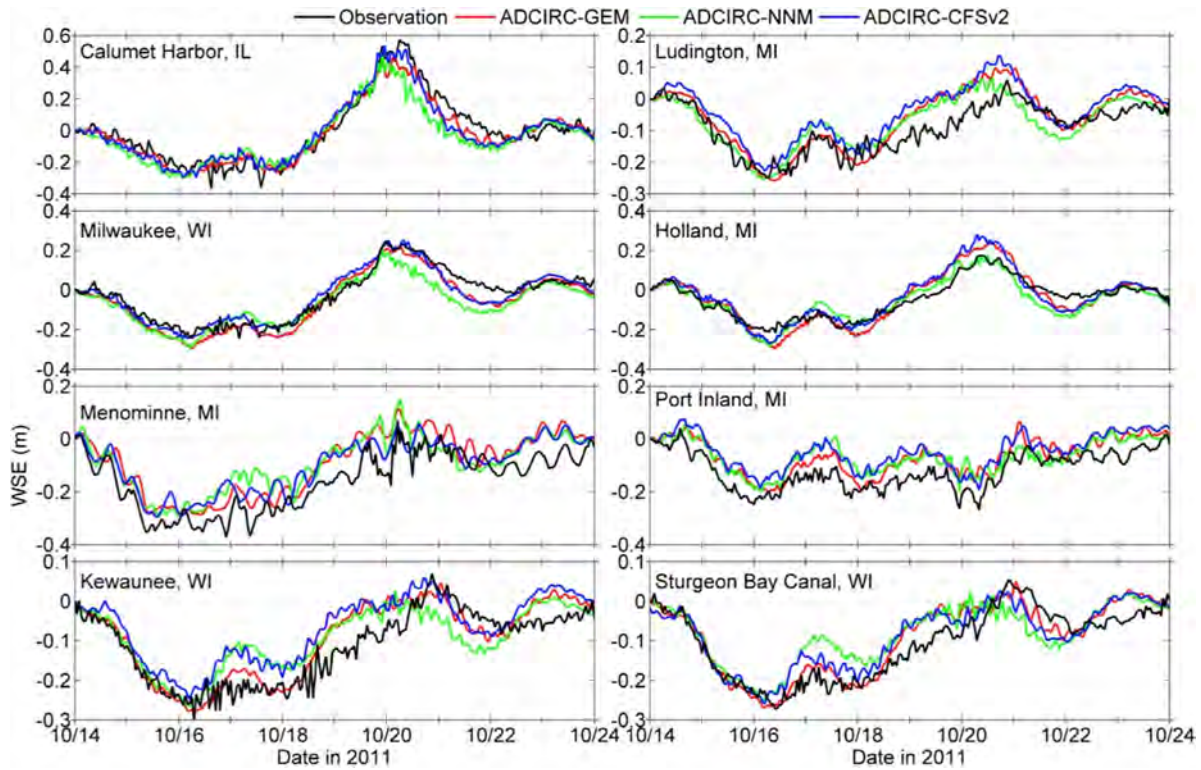
Fig. 2. Time series of WSE produced from ADCIRC by using GEM, NNM, and CFSv2 winds versus observed values at various NOS gauges during October 14–24, 2011.

buoy and meteorological observations (Lang and Leshkevich, 2014; Schwab and Morton, 1984). For the previous studies in the Great Lakes, Jensen et al. (2012) and Hesser et al. (2013) both recommended the adoption of the coupled wind forcing CFSR to replace the observation-based NNM data for the storm surge simulation in Lakes Michigan and St. Clair, respectively. Our findings are consistent with those of Pullen et al. (2007), which made significant improvements on the quantity of the modeled Bora winds over the Adriatic Sea by considering two-way air–sea interactions in the atmosphere–ocean coupled system.

To assess the spatial variability of storm surge resulting from the use of various wind field sources, Fig. 4 shows the spatial wind speed distributions and corresponding WSE fields using these three sources 6 h prior to, during, and 6 h after the surge peak of the 2011 wind event. From north to south, the northeasterly wind increased in intensity progressively, resulting in a similar spatial distribution of the corresponding WSE field. The spatial wind field derived from the atmospheric models (i.e., GEM and CFSv2) showed a more coherent pattern than that from the observation-based NNM winds. It should be noted that the NNM wind field was interpolated from the observational wind data at limited lake buoys and coastal meteorological stations (Jensen et al., 2012; Lang and Leshkevich, 2014) and showed significant spatial and temporal fluctuations. Clearly, the strong CFSv2 wind field led to strong accumulation of the water mass against the large, concave, southwestern coast. When the onshore winds turned toward alongshore or offshore areas in the late period of the storm event, massive amounts of water were forced toward or along the southern and southeastern coasts. This suggests that both the spatial coherence and local steering effect of the wind field are crucial for water transport and storm surge. Even though ADCIRC with the GEM winds showed a slightly better *CC* score for WSE, at 0.93, than that with the CFSv2 winds, at 0.91, the latter reduced the *RMSD* score slightly, from 8.8 cm to 8.5 cm, and improved the *RB* score for surge peak significantly, from −0.21 to −0.13. Although

the wind speed from the GEM model agreed much better with the buoy observation than that from the CFSv2 model, the latter model yielded more accurate consistency with the observed gusty wind (not shown). The effect of severe wind gust, which is not included in the circulation model, is the key factor in predicting storm surge. In addition, the CFSv2 winds are more physically meaningful because they are produced from the two-way atmosphere–ocean fully coupled modeling system. Therefore, the CFSv2 wind product was incorporated into ADCIRC as the default wind forcing for further study, as discussed below.

3.2. Effect of wind drag coefficient bulk formula

After selecting the wind source for the circulation model, the sensitivity studies focused on alternative wind drag coefficient bulk formulae, namely G77 and LP81 for ADCIRC (Cases 1c and 1d) and FVCOM (Case 1f and 1g).

Fig. 5a shows the time series of storm surges produced from Cases 1c–1g versus the observed value at CH, where the most appreciable surge height was recorded during the 2011 wind event. In general, all numerical simulations captured the temporal evolution of the storm surge reasonably well, particularly the 1-h phase lead for the surge peak arrival time. By replacing the LP81 with G77 bulk formula to calculate the wind drag coefficient, both AD-CIRC (Case 1c) and FVCOM (Case 1f) simulated a higher level of storm surge consistently by reducing the *RB* score by half and from −12% to −1%, respectively. When the wind speed was more than 6.7 m/s, the wind drag coefficient calculated from the G77 formulation was expected to be greater than that from the LP81 formulation, as indicated by Eqs. (2) and (6). Accordingly, the enhanced surface wind drag coefficient and the corresponding surface wind stress resulted in stronger storm surge as expected (Weisberg and Zheng, 2008), particularly under strong wind conditions in which the maximum local winds exceeded 15 m/s in the 2011 wind event. In addition, both ADCIRC and FVCOM provided stronger scores of
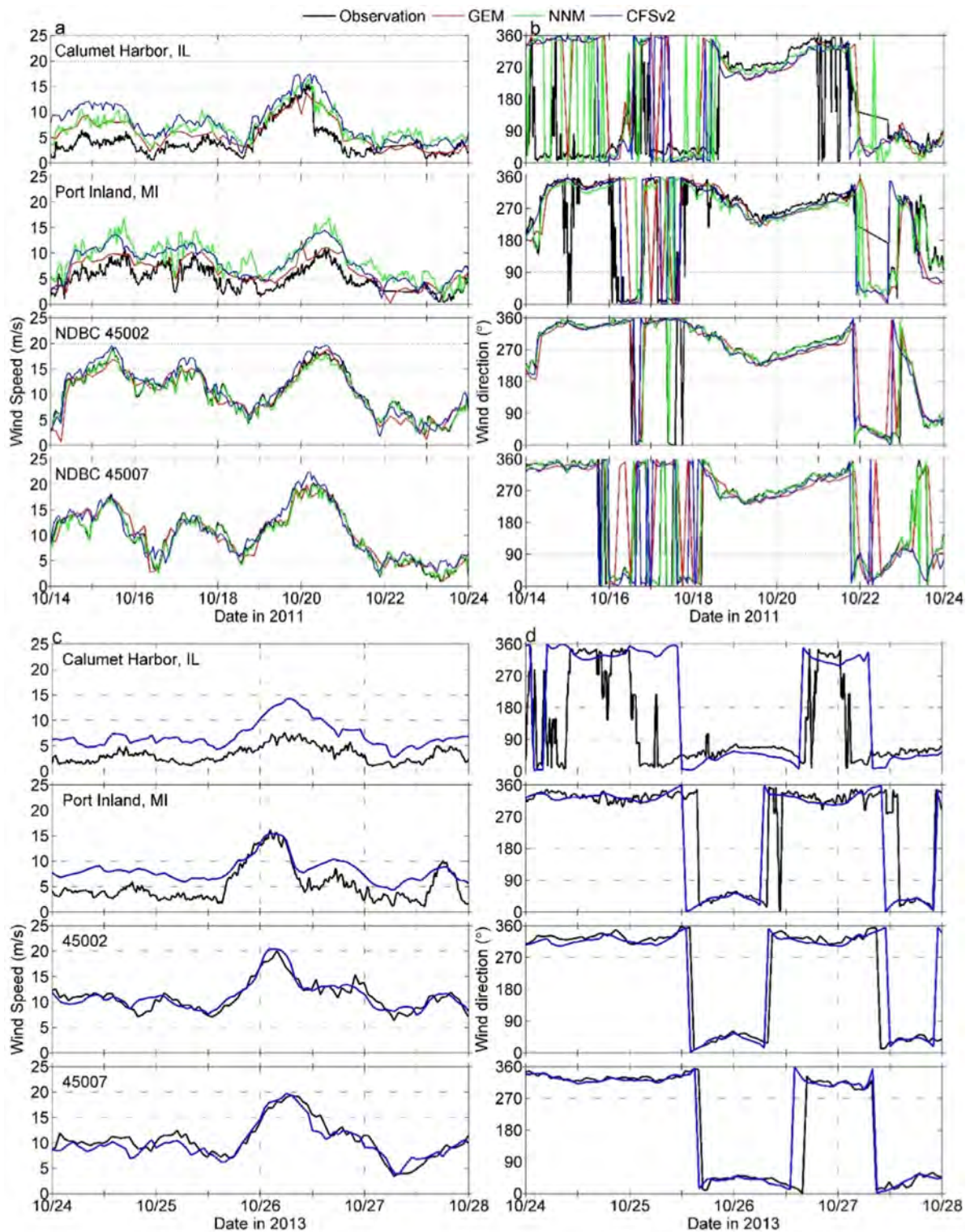
Fig. 3. Time series of (a) and (c) wind speed and (b) and (d) direction retrieved from the GEM, NNM, and CFSv2 fields versus observed values at Calumet Harbor, Illinois and Port Inland, Michigan, and mid-lake buoys 45,002 and 45,007 during (a) and (b) October 14–24, 2011 and (c) and (d) October 24–28, 2013. Only the selected CFSv2 wind field is compared with observation for the 2013 wind event.

RMSD and *CC* for WSE when applying the G77 formulation compared with that of LP81 (Table 2). Therefore, the G77 bulk formula was adopted by ADCIRC and FVCOM as the default setting for calculation of the wind drag coefficient.

3.3. Calibration of SWAN and SWAVE for wave simulation

The recalibrated SWAN (Case 4a in Table 3) adopted the readjusted deep-water wave physics of Rogers et al. (2003), which include the formulations of Janssen (1991) for wind input and Komen et al. (1984) for whitecapping with a dissipation rate of
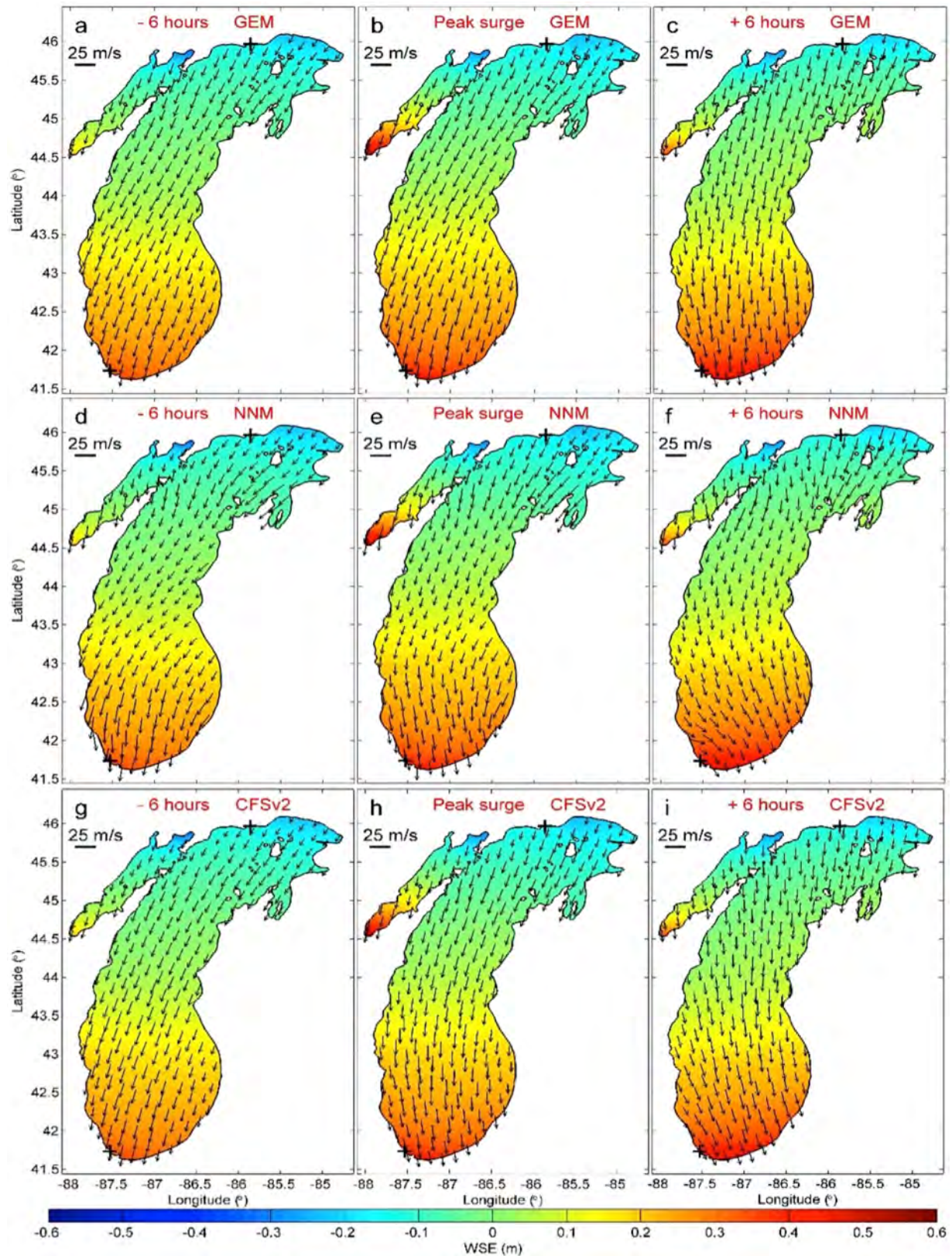
Fig. 4. Images of wind fields (black arrows) and corresponding WSE (colored maps) produced from ADCIRC using GEM (top), NNM (middle), and CFSv2 (bottom) winds 6 h prior to (left), during (middle), and 6 h after (right) the surge peak of the 2011 wind event at 07:00 GMT on October 20. The black crosses at the bottom and top of the panels denote the locations of Calumet Harbor and Port Inland, respectively. (For interpretation of the references to color in this figure legend, the reader is referred to the web version of this article.)
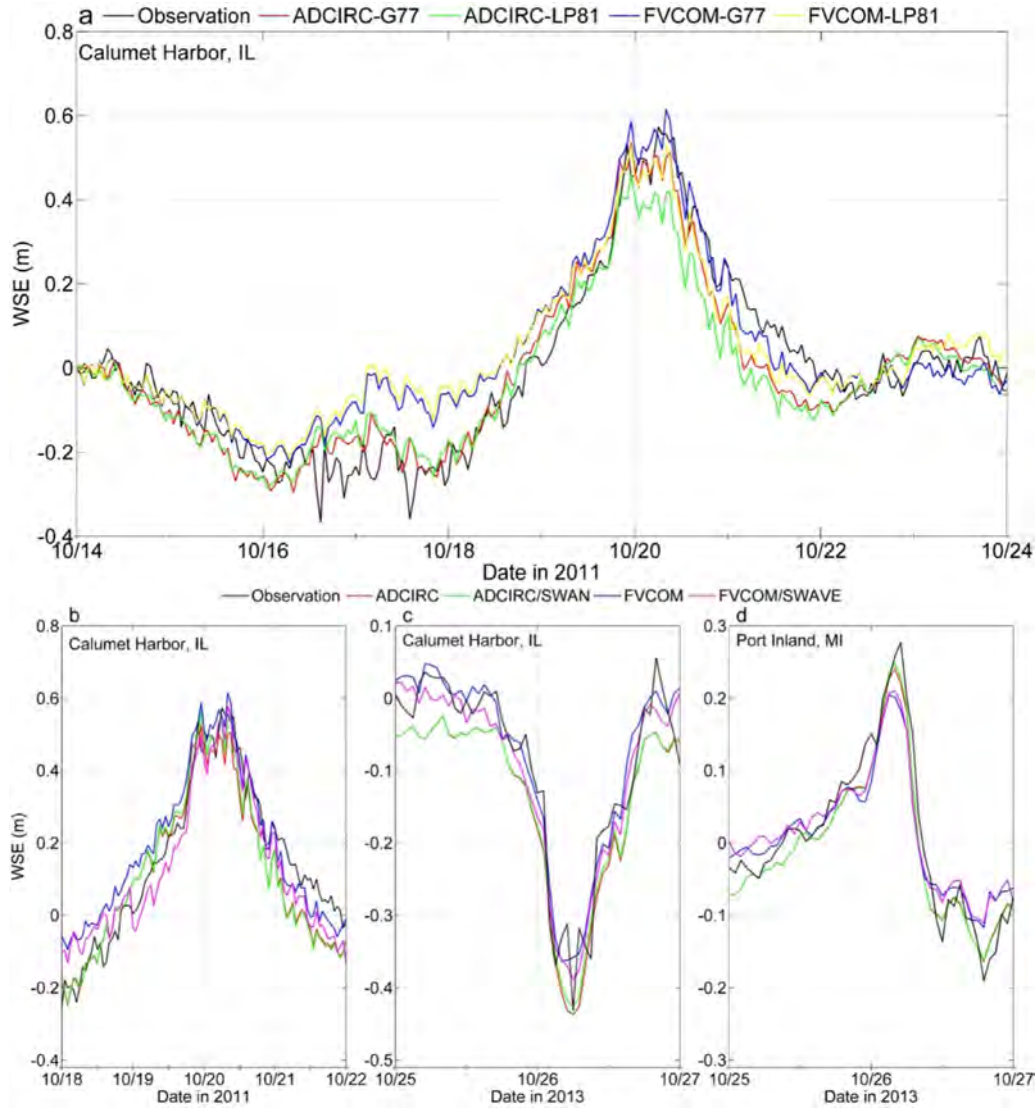
Fig. 5. Time series of WSE produced from (a) ADCIRC and FVCOM with G77 and LP81 bulk formulae of wind drag coefficient versus observed values at Calumet Harbor in the 2011 wind event, and (b)–(d) ADCIRC, ADCIRC/SWAN, FVCOM, and FVCOM/SWAVE with G77 bulk formula versus observed values at Calumet Harbor for the (b) 2011 and (c) 2013 wind events and at Port Inland for the (d) 2013 wind event.

$C_{ds2} = 3 \times 10^{-5}$ and weighting of the relative wave number $\delta = 0.3$. The bore-based breaking model proposed by Thornton and Guza (1983), hereafter referred to as TG83, with a default breaker index of $\gamma_{TG} = 0.42$ was used to account for depth-induced breaking. The bottom friction dissipation and non-linear wave–wave interactions (i.e., triplet and quadruplet) adopted the default settings of SWAN version 40.91 (SWAN Group, 2012a,b). These SWAN settings have been demonstrated as a proper representation of the wave dynamics in Lake Michigan (Mao et al., 2016). Case 4b of SWAVE employed the default formulations of wind input and whitecapping (Komen et al., 1984) in addition to depth-induced breaking reported by Battjes and Janssen (1978), hereafter referred to as BJ78. The recalibrated SWAVE (Case 4c) used the same wave physics settings as those used in the recalibrated SWAN.

Fig. 6a–c show the SWH, PWP, and MWD produced from various wave models (Cases 4a–d; Table 3) versus observed values near the southeastern coast (45,026), in Little Traverse Bay (45,022) and mid-lake area (45,002 and 45,007) during October 14–24, 2011. Despite slight biases for the extreme waves in the mid-lake areas, all cases reproduced the temporal variations of SWH satisfactorily with CC scores not less than 0.93 (Table 4). In addition, they captured the temporal variations of PWP and MWD reasonably well. The PWPs at shallow-water stations 45,026 and 45,022, where the water depths are 21 m and 49 m, respectively, and northern mid-lake station 45,002 were typically below 8.3 s (i.e., wave frequency greater than 0.12 Hz), implying the prevalence of wind–sea conditions (Rogers et al., 2003). In contrast, the wave characteristics in the southern mid-lake area (e.g., station 45,007) were dominated by swell conditions in which the PWP was in the range of 8.3–10 s during October 20–21. This phenomenon can be explained by the fact that the northeasterly winds along the lake's longitudinal axis (i.e., long-fetch conditions) were likely to result in fully developed waves in the southern mid-lake area. The constant but abnormal PWP values (e.g., 1.6 s and 3.0 s) observed at stations 45,026 and 45,022 likely originated from the failure of buoys in capturing the strong shift in wave frequency. As a result of the strong wind–wave–bathymetry interactions, the modeled MWDs in the shallow regions with steep slope near the southeastern coast fluctuated more frequently than those in the deep and smooth mid-lake areas.

Even though Cases 4a and 4c adopted the same wave physics, wave simulations yielded from the FDM-based SWAN and FVM-
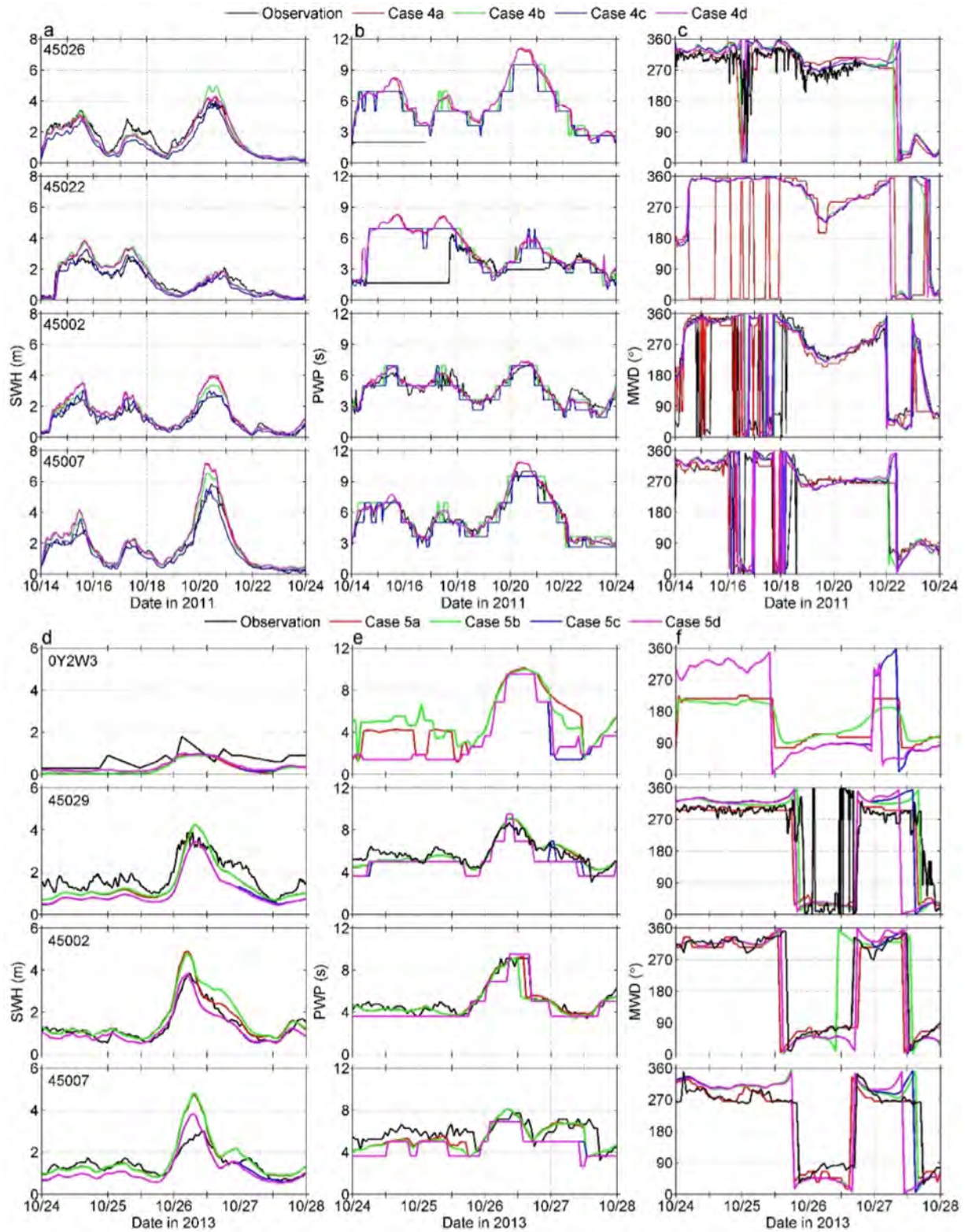
Fig. 6. Time series of (a) and (d) SWH, (b) and (e) PWP, and (c) and (f) MWD produced from (a)–(c) Cases 4a–4d and (d)–(f) Cases 5a–5d versus observed values at various NDBC buoys during (a)–(c) October 14–24, 2011 and (d)–(f) October 24–28, 2013. Detailed settings of Cases 4a–5d are given in Table 3.

based SWAVE differed (Fig. 6a–c; Table 4), presumably owing to different discretization algorithms. It is clear that the modification of wave physics settings in SWAVE from Cases 4b to 4c resulted in improved estimation of the wave parameters (e.g., the ensemble of *RMSD* score was reduced by 7%), especially for the peak SWH in

the mid-lake areas (e.g., stations 45,002 and 45,007). Therefore, the physically meaningful tuning strategy (Rogers et al., 2003) in Cases 4a and 4c were incorporated into SWAN and SWAVE, respectively.

Table 4
MSD and *CC* scores for SWH from the designed numerical experiments for SWAN and SWAVE and the *MAV* and *SDAV* for the observed SWH.

| Simulation Period	Case/Station	RMSD (m)				CC				Observation	
		4a	4b	4c	4d	4a	4b	4c	4d	MAV (m)	SDAV (m)
2011 October 14–24	45,026	0.43	0.52	0.67	0.46	0.94	0.93	0.94	0.93	2.12	0.89
	45,022	0.40	0.44	0.32	0.41	0.95	0.95	0.95	0.95	1.24	0.80
	45,002	0.42	0.33	0.23	0.43	0.95	0.97	0.96	0.95	1.09	0.63
	45,007	0.52	0.39	0.33	0.52	0.97	0.98	0.98	0.98	1.47	1.30
	Average	0.44	0.42	0.39	0.46	0.95	0.96	0.96	0.95	1.48	0.90
2013 October 24–28	Case/Station	5a	5b	5c	5d	5a	5b	5c	5d	Observation	
	0Y2W3	0.50	0.48	0.42	0.41	0.67	0.67	0.66	0.69	0.72	0.38
	C58W3	0.36	0.34	0.34	0.34	0.53	0.55	0.56	0.54	0.54	0.36
	45,170	0.59	0.61	0.81	0.81	0.53	0.50	0.38	0.43	1.45	0.44
	45,029	0.57	0.56	0.79	0.80	0.89	0.88	0.88	0.89	1.79	0.82
	45,161	0.23	0.24	0.36	0.36	0.97	0.97	0.97	0.97	1.42	0.89
	45,024	0.42	0.42	0.61	0.62	0.93	0.93	0.93	0.93	1.81	0.67
	45,002	0.40	0.48	0.32	0.31	0.95	0.96	0.94	0.95	1.38	0.82
	45,007	0.55	0.57	0.45	0.46	0.90	0.90	0.89	0.89	1.44	0.55
	Average	0.45	0.46	0.51	0.51	0.80	0.79	0.78	0.79	1.32	0.62
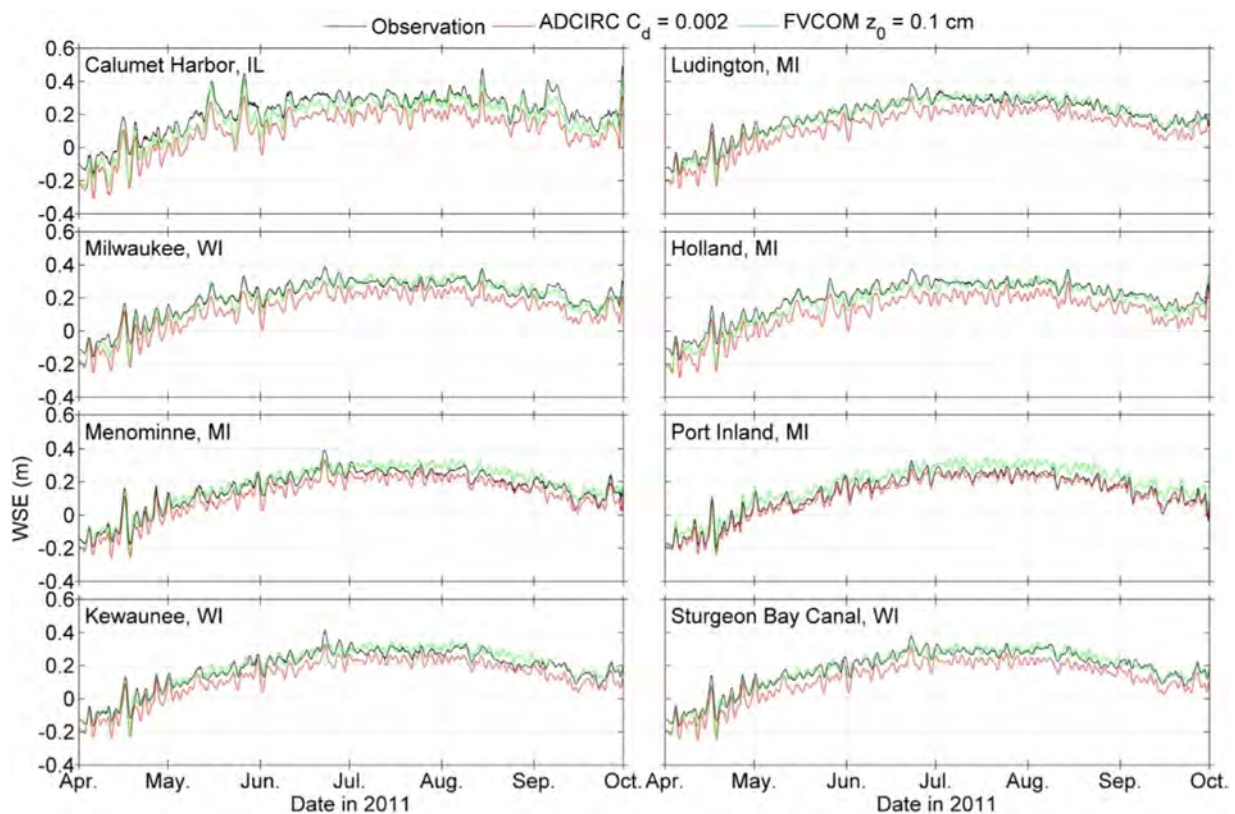
Fig. 7. Time series of WSE produced from ADCIRC with a bottom drag coefficient of 0.002 and FVCOM with a bottom roughness length of 0.1 cm versus observed values at various NOS gauges in April–October 2011.

3.4. Calibration of water surface elevation simulation

Kerr et al. (2013a) reported that parameterization of the bottom friction term is crucial for the WSE and storm surge simulations. In this study, sensitivity experiments using bottom drag coefficients of 0.002, 0.0025 (used for Lake Erie by O'Connor et al., 1999), and 0.003 (used for the Gulf of Mexico by Kerr et al., 2013a) in AD-CIRC (Cases 2a–2c), and bottom roughness lengths of 0.1 cm (used for Lake Michigan by Beletsky et al., 2003, 2006), 0.5 cm, and 1 cm (used for Lake Michigan by Beletsky and Schwab, 2001 and Schwab et al., 2000) in FVCOM (Cases 2d–2f) were examined, respectively. Fig. 7 shows the time series of WSE produced from ADCIRC with a bottom drag coefficient of 0.002 (Case 2a) and from FVCOM with a bottom roughness length of 0.1 cm (Case 2d) versus observed values at eight NOS stations over the period April–October 2011. Both circulation models (i.e., ADCIRC and FVCOM) with different parameterizations of the bottom friction term reproduced the temporal variations of WSE fairly well. It should be noted that FVCOM estimated a consistently higher level of WSE than that of ADCIRC and yielded a smaller bias relative to observations (e.g., $RMSD \leq 4.5$ cm versus $RMSD \geq 7.1$ cm). However, ADCIRC provided a slightly better *CC* score than that of FVCOM within the simulation period, at 0.98 versus 0.96–0.97. The time series of WSE produced from ADCIRC (FVCOM) with different bottom drag coefficients (bottom roughness lengths) were very similar and almost overlapped (figures not shown); the *CC* and *RMSD* scores for WSE

produced from Cases 2a–2c were 0.98 and about 7 cm, respectively (Table 2). On average, Cases 2a ($RMSD = 7.1$ cm and $CC = 0.98$) and 2d ($RMSD = 4.0$ cm and $CC = 0.97$) provided the best statistical scores for the WSE simulation of ADCIRC and FVCOM, respectively. Therefore, they were adopted as default parameterizations of the bottom drag coefficient and bottom roughness length in ADCIRC and FVCOM, respectively.

4. Validation case: southwesterly wind event in october 2013

Swineford et al. (2014) examined three successive autumn storms that passed over Lake Michigan from October 24 to November 6, 2013. The first southwesterly storm, occurring October 24–28, generated the highest wind speed of 16.7 m/s and strongest SWH of 2.8 m near the mid-eastern coast. This case was selected as the validation experiment for this section.

Fig. 6d–f show the time series of SWH, PWP, and MWD produced from two wave models with and without WCSI (Cases 5a–5d; Table 3) versus observed values at NDBC stations near the northwestern (0Y2W3) and mid-eastern (45,029) coasts in addition to the mid-lake area (45,002 and 45,007) during October 24–28, 2013. All simulations reproduced the temporal evolution of SWH satisfactorily, despite a somewhat underestimation near the mid-eastern coast and an overestimation in the southern mid-lake area. Consistent overestimations of SWH were found in the open water at a large distance from the shore, particularly in extreme waves at station 45,007. This result was likely caused by overestimation of the momentum transfer from surface winds to the fully developed waves under strong wind conditions while ignoring the air–sea flow separation effect in the conventional wind input formulation adopted by current wave models (Donelan et al., 2006). Even though the local winds produced from the CFSv2 model agreed well with observations, overestimation of remote winds near the coast can lead to amplification of the modeled SWH in the mid-lake area, such as northward propagation of swell generated by the strong southwesterly winds around October 26 (Figs. 3c,d and 6d–f). The consistent SWH difference between SWAN (Case 5a) and SWAVE (Case 5c), particularly under extreme wave conditions, may be attributed to the adoption of different numerical schemes and discretization algorithms (Chen et al., 2013). Driven by the southwesterly winds, swell conditions (e.g., low PWP or high wave frequency) developed progressively in the northern mid-lake area due to the enhanced wind fetch distance along the longitudinal axis of the lake. Compared with the results from SWAVE, SWAN slightly improved the averaged scores of $RMSD$ and CC for SWH (Table 4) and followed the temporal trends of PWP better (Fig. 6e). By coupling the hydrodynamic model with the wave model, Dodet et al. (2013) determined that the current–wave effects (e.g., modulations of SWH) were pronounced within extremely shallow tidal inlet regions. However, this improvement is trivial in the deep waters of Lake Michigan owing possibly to weaker variations in current velocity and water depth, particularly a lack of strong tidal currents and flooding and drying processes. To assess the spatial differences in SWH produced from different wave models, Fig. 8 presents the SWH field produced from SWAN and the percentage difference of SWH between SWAN and SWAVE relative to the SWAN result at the surge peak of the 2013 wind event at 06:00 GMT on October 26. Spatially, large waves 5–6 m in estimated height developed gradually in the downwind region, which was followed by intensive depth-induced breaking in close proximity to the eastern and northern coasts and islands. Overall, the relative difference in SWH produced from SWAVE and SWAN was less than 40% in the center region of southern mid-lake area. However, the absolute SWH difference between the paired circulation models was relatively large, at 1.5–2 m, owing to the high SWH value in this region.

Fig. 5b–d show the time series of WSE covering the surge peak produced from various circulation models versus observed values at CH during the 2011 wind event and at CH and PI during the 2013 wind event. Fig. 3c and d show the time series of wind speed and direction produced from the default wind forcing (i.e., CFSv2) versus observed values at CH, PI, and mid-lake stations 45,002 and 45,007 during the 2013 wind event. The observed wind began to increase in intensity on October 26, 2013, resulting in 0.28 m setup at PI and –0.43 m setdown at CH. The magnitudes of setup and setdown were underestimated by 26% and 16% from FVCOM (Case 3c), which were reduced to half and 1% from ADCIRC (Case 3a), respectively. Statistically, FVCOM provided a smaller score of $RMSD$ for WSE, at 5.8 cm, than that of ADCIRC, at 6.7 cm. The different results produced from ADCIRC and FVCOM can be attributed to the distinct discretization algorithms and bottom friction formulations (Chen et al., 2013). Overall, the wind speed derived from the CFSv2 model was consistently higher than that from the buoy observation at CH; however, the calculated storm surge was close to observed value. Because strong, gusty winds are significant for the prediction of storm surge, they should be considered in the current circulation model. Therefore, incorporation of wind gust, which was well reproduced by the CFSv2 model (not shown), into the circulation model is likely to be more realistic. Fig. 9a–b show images of WSE produced from ADICRC and the WSE difference between ADCIRC and FVCOM at the surge peak of the 2013 wind event. The southwesterly winds (Fig. 3c and d) transported massive amounts of water to the northern mid-lake area, resulting in great setups near the northern coast of Lake Michigan and Green Bay, at 30–40 cm and 20–30 cm, respectively. Consequently, the WSE differences between Cases 3a and 3c in these regions, at 10–15 cm, were larger than those in the mid-lake area, at 0–10 cm.

5. Results and discussion

5.1. Effects of WCSI on storm surge and wave dynamics

Given the importance of WCSI, their effects on storm surge were investigated (Fig. 5b–d). During the 2011 wind event, the arrival time of the storm surge predicted by ADCIRC both with (Case 1e) and without WCSI (Case 1c) led the observation by 1h. However, the model-to-data discrepancy of the storm surge (i.e., RB for setup at CH) was reduced from –13% to –6% in ADCIRC by including WCSI; this was presumably caused by wave-induced setup related to WRS gradients (Dodet et al., 2013). It should be noted that FVCOM estimated the storm surge at CH with nearly perfect precision with or without WCSI for the 2011 wind event. For the 2013 wind event, the underprediction of the setup was reduced slightly by 3% in ADCIRC and 2% in FVCOM owing to the inclusion of WCSI. The RB score for setdown in FVCOM was slightly improved from –0.16 to –0.10 by including the wave effects. With the inclusion of WCSI, the WSE simulation was only slightly improved and at times even deteriorated marginally; CC was 0.91 and 0.90 for Case 1c and Case 1e, respectively. This phenomenon is attributed to relatively weak intensity of wind and waves under normal conditions (e.g., the $RMSD$ and CC scores for WSE) compared with those at the surge peak of storm events (e.g., RB score for storm surge). Consequently, the effect of WCSI on the magnitude of the peaked storm surge during a particularly strong wind event was larger than that for WSE over longer periods of ten and four days for the 2011 and 2013 wind events, respectively.

To study the effect of WCSI on storm surge spatially, the images of the WSE differences between ADCIRC/SWAN and ADCIRC at the surge peaks of the 2011 and 2013 wind events at 07:00 GMT on October 20 and 06:00 GMT on October 26, respectively, are presented in Fig. 9c and d. In the 2011 wind event, the WSE difference between Cases 1e and 1c (e.g., 1–5 cm) were most evident in the
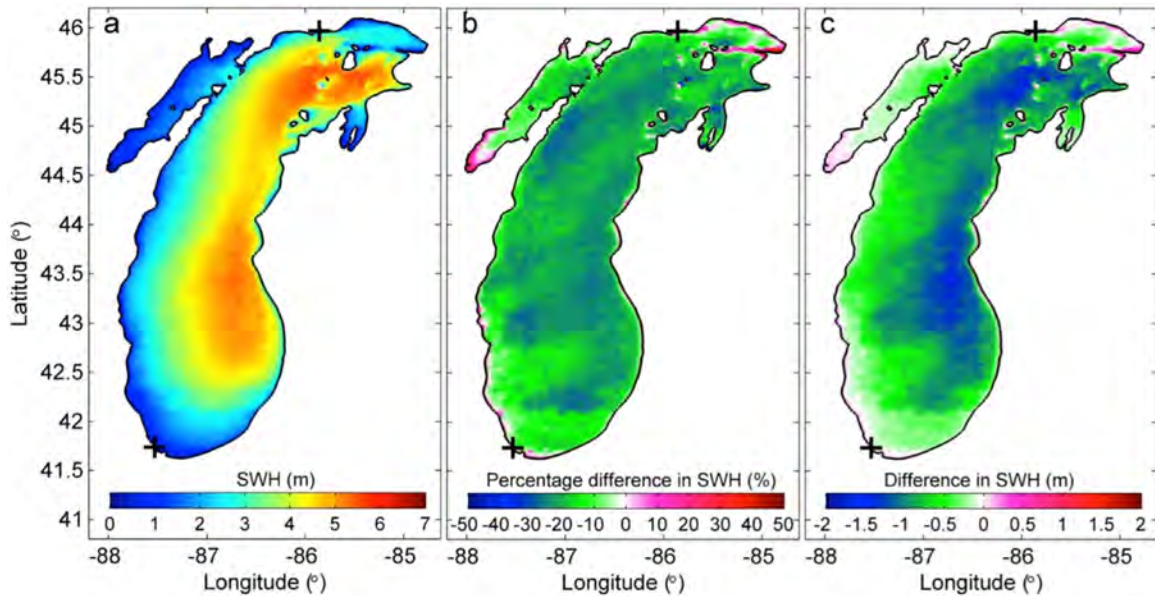
Fig. 8. Images of (a) SWH produced from SWAN, and the modeled SWH difference between SWAN and SWAVE in (b) percentage relative to the SWAN result and (c) absolute value at the surge peak of the 2013 wind event at 06:00 GMT on October 26. The black crosses at the bottom and top of the panels denote the locations of Calumet Harbor and Port Inland, respectively.

downwind regions near the coast, which was presumably caused by the wave-induced setup/setdown. This result supports the conclusion drawn by Roland et al. (2009) that the wave breaking process along the coast and islands affects WSE variations significantly during storm events. For the Lake Michigan simulation, Jensen et al. (2012) postulated that the wave-induced setup in Green Bay could reach 10–20 cm under specific conditions. During both wind events, the model's performance was generally improved by incorporating WCSI into the circulation models. Even though this improvement was relatively small compared with the difference between alternative WCSI-coupled modeling systems, this physically meaningful process was incorporated into the modeling system considering its consistent contribution to the improvement of model accuracy. Moreover, the two model systems were similar to each other (i.e., independent of WCSI) although some differences were noted with the data. The consistent model-to-data discrepancy is possibly caused by the inaccuracies of external wind forcing (e.g., wind speed and wind direction). Therefore, future research should consider improving the numerical accuracy by reconstructing the wind field by appropriate blending of modeled and buoy-based wind data (He et al., 2004).

Wave radiation stress is a primary contributing force for wave-induced setup/setdown (Dodet et al., 2013; Kerr et al., 2013a). In order to investigate other wave effects on storm surges and currents, additional numerical experiments based on the default 2D WCSI-coupled FVCOM/SWAVE (Case 3d) were conducted. Cases 3e–3h excluded the wave effects on bottom stress, sea surface roughness, and Stokes current and include breaking-induced momentum injection, respectively. Analysis of the simulation results indicates that these additional wave effects on storm surge, such as the phase and magnitude of the surge peaks at CH and PI stations, are negligible (not shown). Based on the images of depth-averaged current velocity differences at the surge peak of the 2013 wind event induced by the corresponding wave effects, we find that these wave effects on the depth-averaged current velocity occur mainly around the islands in the northern basin and near the coasts with less than 2 cm/s variations (figures not shown). Liu and Xie (2009) reported that the wave effects on storm surge

through surface wind stress and bottom friction are important in the small and shallow Charleston Harbor, South Carolina. Subsequently, Röhrs et al. (2012) addressed the significant effects of surface waves on currents by using the wave-induced momentum and TKE flux in addition to Stokes drift in the water surface layer at the coast of Nordland, Norway. For the large and deep Lake Michigan domain with a regional scale of O (100 km), however, these wave effects on storm surge and depth-averaged current are quite weak and can be ignored (not shown). Therefore, the default configurations for the wave effects on the circulation model in the 2D barotropic FVCOM/SWAVE (Case 3d) and ADCIRC/SWAN (Case 3b), which is similar to Case 3d but does not include the wave-induced bottom roughness length and Stokes drift, are appropriate. It is beyond the scope of present study to address the interaction of these wave effects with 3D baroclinic motions.

To investigate the effect of WCSI on wave dynamics, wave simulations produced from the wave-only models were compared with those from the corresponding WCSI-coupled models. Previous studies have indicated that the influence of WCSI on waves is mainly through the processes of current-induced wave refraction and frequency shift (Benetazzo et al., 2013; Hopkins et al., 2016; Wolf and Prandle, 1999) in addition to depth-induced wave breaking (Liu and Xie, 2009). The modifications of PWP near the northwestern coast (0Y2W3) and MWD near the eastern coast (45,026 and 45,029) by currents are clearly seen in Fig. 6. With the inclusion of WCSI, the relative model-to-model differences in SWH (i.e., the modeled SWH from ADCIRC/SWAN minus SWAN divided by that from ADCIRC/SWAN) near the southern coast of Green Bay and Lake Michigan and near Beaver Island were up to 20% (Fig. 9e and f). Because the SWH in shallow waters is modulated by local water depth (i.e., depth-induced breaking), its variation is heavily dependent on the intensity of storm surge in these regions (Liu and Xie, 2009). Chen et al. (2013) demonstrated a significant modulation effect of local water depth on SWH in the shallow Scituate Harbor, particularly during extratropical storms with frequent flooding and drying processes. It should also be mentioned that the relative difference in SWH caused by WCSI was smaller than that resulting from the use of different WCSI-coupled models
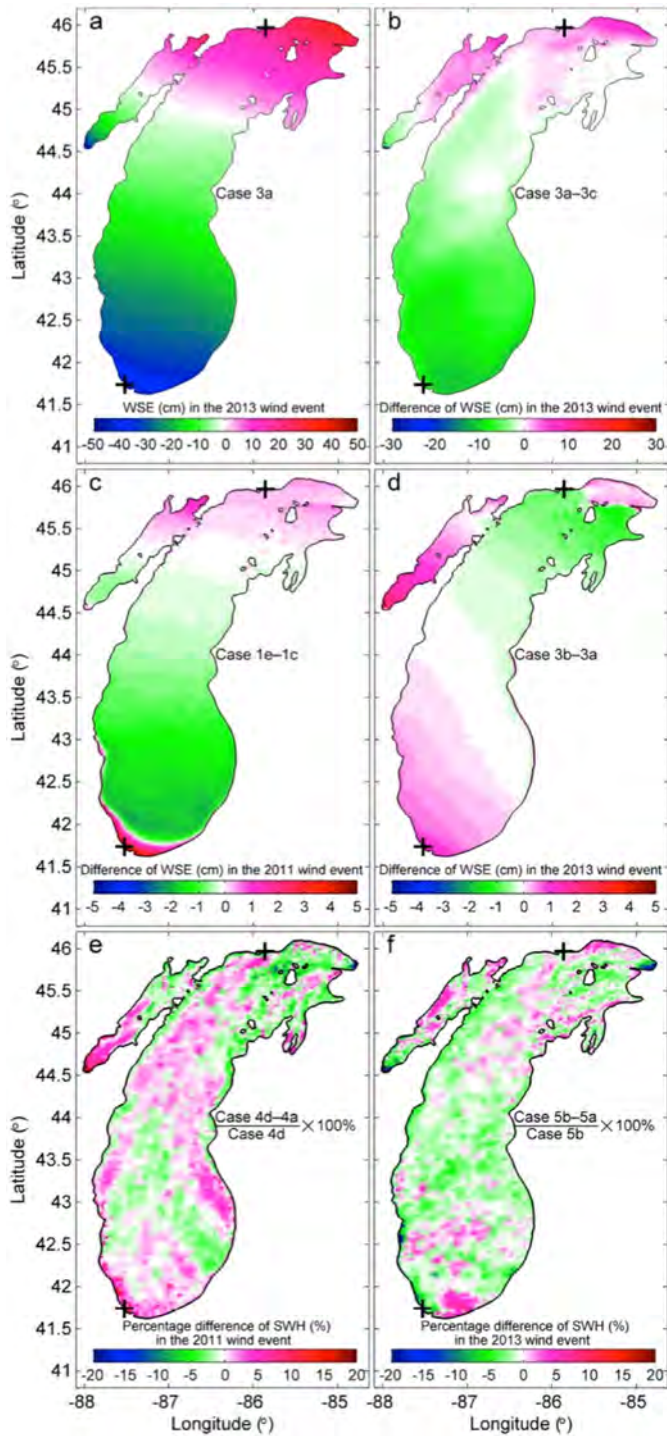
Fig. 9. Images of (a) WSE produced from ADCIRC and the modeled WSE difference (b) between ADCIRC and FVCOM at the surge peak of the 2013 wind event at 06:00 GMT October 26, and (c)–(d) between ADCIRC/SWAN and ADCIRC at the surge peak of (c) the 2011 wind event at 07:00 GMT on October 20 and (d) 2013 wind event at 06:00 GMT on October 26. Panels (e) and (f) are the same as (c) and (d), respectively, except for the SWH differences in percentage between ADCIRC/SWAN and SWAN. The black crosses at the bottom and top of the panels denote the locations of Calumet Harbor and Port Inland, respectively.

(Figs. 8b and 9f). Considering the dominant influence of prevailing winds on currents in a semi-enclosed basin (Benetazzo et al., 2013), we further explore the manner in which storm surge develops under the synergistic effects of strong winds and coastal geometry and bathymetry in the following subsection.

5.2. Dynamic response of water transport to wind forcing

Fig. 10 shows the DWTFs of lake–lake (Lakes Michigan and Huron), basin–basin (Chippewa Basin and South Chippewa Basin), basin–bay (Lake Michigan and Green Bay, and Lake Michigan and Grand Traverse Bay), and area–area (lower and upper Green Bay) during a 6-h period prior to the surge peaks of the 2011 and 2013 wind events. For the 2011 wind event, the downwind and upwind portions of DWTF across the mid-lake transect were nearly setoff from each other with a net DWTF of –4650 m^3/s. This result may have been caused by the enclosed nature of the southern coast, which generates return flow owing to the wall effect. This process corroborated a recent finding of McCombs et al. (2014), who reported that a return circulation in the middle of the enclosed Lake Ontario was generated to compensate for the onshore flow under spatially uniform wind conditions. It is noted that the net DWTF across the Straits of Mackinac (21,187 m^3/s) resulted in a large amount of water transport in the 2011 wind event, which implies that the inclusion of lake–lake water exchange in the circulation model is important to lake dynamics (Anderson and Schwab, 2013; Jensen et al., 2012). A large amount of water from the major portion of the lake flows into Green Bay (17,914 m^3/s), and more than one third of the inflow (–7112 m^3/s) further moves southwardly inside the bay. Driven by the long-fetch winds over the narrow and elongated Green Bay, a massive amount of water piles up against the southern coast of the bay. Because of the short fetch distance and lower inflows (3489 m^3/s), the enhancement of WSE is nearly spatially uniform over the deep Grand Traverse Bay (Fig. 4).

When the southwesterly winds are predominant over the lake, the coastal boundary in the downwind region is semi-enclosed; an open boundary connects with Lake Huron. Because of significant outflow into Lake Huron, the amount of lateral return flows is smaller than that during the northeasterly wind event. In the 2013 wind event, the downwind flow across the mid-lake transect significantly exceeded the return flow; the net basin–basin DWTF was 96,008 m^3/s. This amount is more than twice that reported in Lake Winnipeg during a storm event in October 2010, which was less than 40,000 m^3/s (Chittibabu and Rao, 2012). Compared with the size and average depth of Lake Michigan, Lake Winnipeg is relatively small and shallow with a surface area of 24,514 km^2 and average depth of 12 m. Additionally, a narrow channel 2.5 km in width separates the northern and southern basins of Lake Winnipeg. Therefore, the different flow amounts and directions between these two lakes result from different synergistic effects of wind direction, wind speed, and basin morphology. For the 2013 wind event, nearly half of the basin–basin flux, –42,403 m^3/s, was diverted into the Straits of Mackinac, leading to a relatively lower setup of 0.28 m than that in the 2011 wind event at 0.57 m. Owing to the site-specific features of coastal geometry and bathymetry, the amount of basin–bay DWTF via Green Bay, at –12,818 m^3/s, is significantly higher than that via Grand Traverse Bay, at –986 m^3/s.

To investigate the influence of return flow from lateral and deep water and that of baroclinic oscillation on the evolution of storm surge, the depth-averaged current fields produced from 2D ADCIRC/SWAN and FVCOM/SWAVE and 3D barotropic and baroclinic FVCOM/SWAVE during a 6-h period prior to the surge peak of the 2013 wind event were examined (Fig. 11). Owing to the stronger northward and southward currents detaching from the anti-cyclonic (i.e., clockwise) eddy in the southern mid-lake area, ADCIRC/SWAN transported larger amounts of water and produced a higher magnitude of setup and setdown near the lake's northern and southern coasts than those from 2D FVCOM/SWAVE. Considering the effect of deep-water return flow on the depth-averaged current velocity field, both 3D FVCOM/SWAVE models yielded relatively stronger depth-averaged flows along the southwestern and
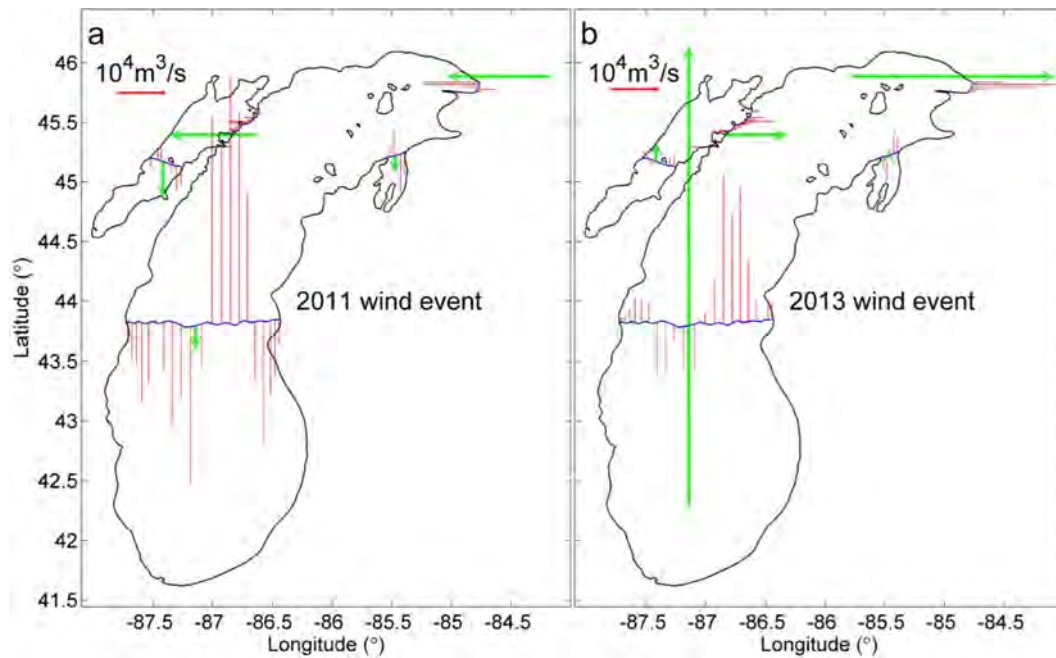
Fig. 10. Vector representation of the DWTF produced from ADCIRC/SWAN during a 6-h period before the surge peak of the (a) 2011 and (b) 2013 wind events. The red solid lines and green arrows refer to the DWTF through the meshes and the entire transect, respectively.

southeastern coasts and into the Straits of Mackinac compared with the results from 2D FVCOM/SWAVE. Accordingly, the 3D barotropic model resulted in greater setdown (–0.43 m; $RB = -0.01$) and lower setup (0.18 m; $RB = -0.34$). Even though the vertical variations of current velocity in the surface and middle layers (not shown) from the 3D baroclinic model, at 60 cm/s, were significantly larger than that from the 3D barotropic model, at 20 cm/s, both models produced similar depth-averaged current fields. When the baroclinic process was included, the RB scores for setup (–0.27) and setdown (–0.07) were slightly improved and deteriorated, respectively. Therefore, the 2D barotropic version of FVCOM/SWAVE was applied in this study. However, the 3D circulation pattern detected in the baroclinic model suggests that this has very important consequences for ecological issues, such as sediment resuspension, transport, erosion, and the spatial distribution of biological fields (Chen et al., 2004).

It should be mentioned that the simulation with the 3D baroclinic model is a very rudimentary test concerning the potential consequences of baroclinic motions because three sigma layers are not sufficient for representing stratification in a reasonable manner. Improvement of the hydrodynamic simulation in Lake Michigan has been partially achieved by refining the vertical resolution and by providing more accurate initial conditions from the Princeton Ocean Model (POM) by Beletsky et al. (2006). However, sigma-layer-based models (e.g., FVCOM and POM) may still lead to poor predictions of baroclinic motions in lakes (Niu et al., 2015) because the stratification is horizontally rather uniform, and the layers in a model with a sigma coordinate system in the vertical direction typically are not well oriented with respect to isopycnals (Mellor et al., 1994, 1998). Because inclusion of the 3D baroclinic process amplified the velocity difference between the surface and bottom layers three times, it is expected that this change can substantially increase the results of current–wave effects (Kirby and Chen, 1989). However, the development of a very well designed 3D WCSI-coupled baroclinic model for accurate wave and surge simulations is beyond the scope of this manuscript.

6. Summary of findings and study conclusions

This study configured a pair of WCSI-coupled modeling systems to Lake Michigan based on the hindcasts of two strong but distinct wind events. To investigate the effects of WCSI on storm surge and wave dynamics, simulations with and without WCSI were inter-compared by using observations from NOS gauges and NDBC buoys. Various responses of the paired circulation (ADCIRC and FVCOM) and wave models (SWAN and SWAVE) to strong wind events were examined. The results are summarized in the following points.

(1) ADCIRC driven by the CFSv2 model provides better skill in storm surge simulation than that using the GEM or NNM wind field likely because the CFSv2 wind field is the only source produced from a two-way atmosphere–ocean fully coupled modeling approach. Modeled storm surges from both ADCIRC and FVCOM agree better with observations when replacing the LP81 with the G77 bulk formula of wind drag coefficient. For the 2011 wind event, the calibrated ADCIRC (Case 1c) and FVCOM (Case 1f) underestimated the setup at CH by 13% and 1%, respectively. For the 2013 wind event, the observed setup (setdown) at PI (CH) was biased by –13% (1%) and –26% (–16%) from ADCIRC and FVCOM, respectively.

(2) Wave-induced setup (setdown) is primarily caused by WRS gradients, which influence storm surge in the downwind (upwind) region adjacent to the coast. The observed setup for the 2011 wind event (0.57 m) and setdown in the 2013 wind event (–0.43 m) were nearly perfectly replicated by FVCOM ($RB = -0.01$; 0.4 cm underestimation) and ADCIRC ($RB = 0.01$; 0.6 cm overestimation), respectively. For the 2013 wind event, ADCIRC and FVCOM underestimated the observed setup (0.28 m) by 13% (3.6 cm) and 26% (7.3 cm), respectively. With the inclusion of WCSI, ADCIRC reduced the underpredicted setups from 13% (7.4 cm) to 6% (3.4 cm) and from 13% (3.6 cm) to 10% (2.8 cm) for the 2011 and 2013 wind events, respectively; FVCOM reduced the underestimated setup and setdown from 26% (7.3 cm) to 24% (6.7 cm) and from 16% (6.9 cm) to 10% (4.3 cm) for the 2013 wind event. When including WCSI in the circu-
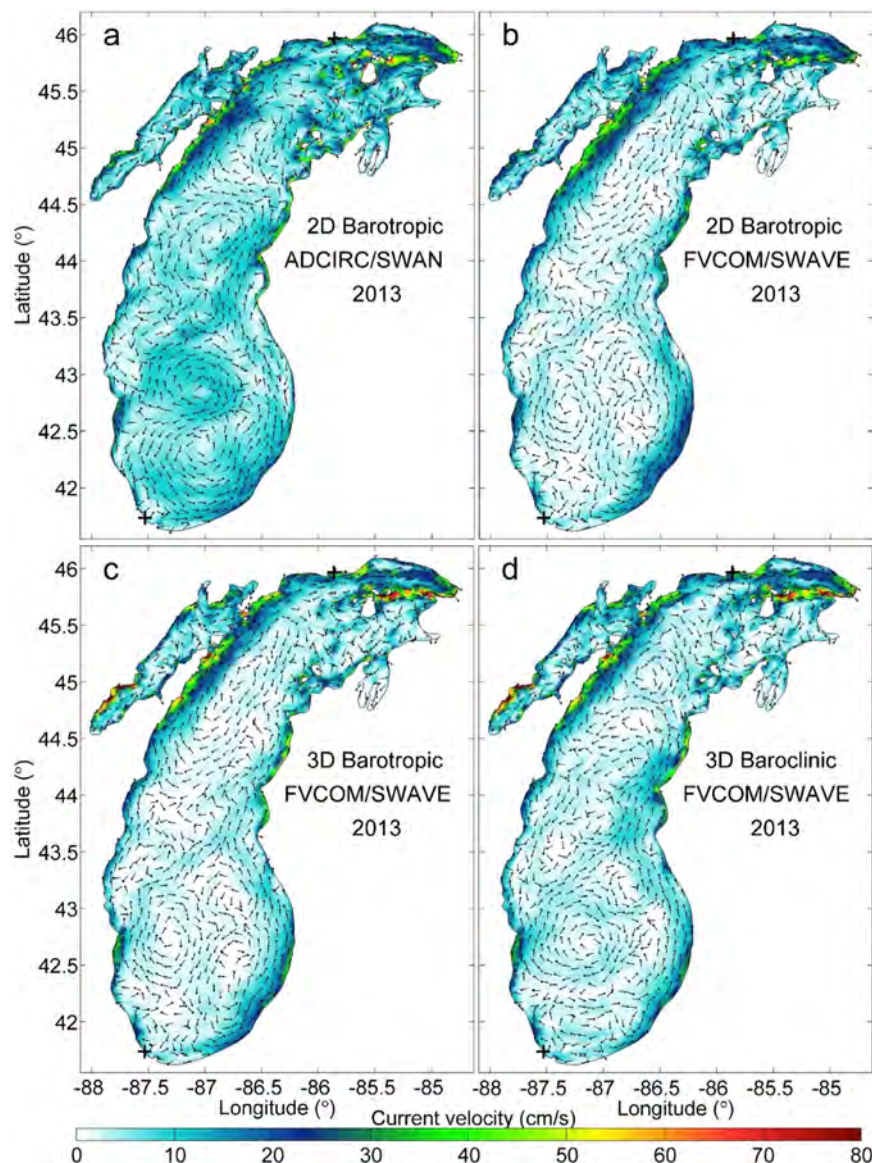
Fig. 11. Depth-averaged current fields produced from (a) 2D ADCIRC/SWAN and (b) FVCOM/SWAVE, and (c) 3D barotropic and (d) baroclinic FVCOM/SWAVE during a 6-h period prior to the surge peak of the 2013 wind event at 06:00 GMT on October 26. The black crosses at the bottom and top of the panels denote the locations of Calumet Harbor and Port Inland, respectively.

lation models, the model skill in simulating WSE improved slightly with occasional and marginal deterioration of the *CC* score (e.g., Cases 1c and 1e).

(3) WCSI affects wave dynamics through depth-induced breaking, and current-induced frequency shift and refraction in the shallow-water regions near coasts and islands. With the inclusion of WCSI, improvement in the modeled SWH for shallow-water stations such as 0Y2W3 and C58W3, where water depths are 5–6 m, was trivial (e.g., the *RMSD* score for SWH at both stations in Table 4) compared with that in extremely shallow regions such as Scituate Harbor, where the variations in current velocity and water depth are strong and frequent (e.g., flooding and drying processes). Relative to the WCSI effects, the modeled SWH was more sensitive to the descriptions of deep- and shallow-water wave physics and the selection of the modeling system with the use of alternative discretization algorithms and bottom friction formulations.

(4) The magnitude of the storm surge is associated with wind speed, wind direction, and coastal geometry and topography. For the 2011 wind event, the large, concave shape of the en-closed southwestern coast caused a massive amount of wind-driven water to accumulate against the coast. For the 2013 wind event, the presence of the Straits of Mackinac diverted a large portion of water from Lakes Michigan to Huron. The shallow and elongated Green Bay facilitates stronger WSE variations against the coast, whereas the deep and short Grand Traverse Bay impedes wind growth and results in spatially coherent WSE variations.

The configuration of ADCIRC/SWAN and FVCOM/SWAVE to Lake Michigan indicates the applicability of the WCSI-coupled 2D barotropic models to a regional-scale O (100 km) semi-enclosed domain. The work conducted in this study is useful for understanding the WCSI processes in other lakes. The rudimentary simulation results from the WCSI-coupled 3D barotropic and baroclinic models suggest that the investigation of baroclinic motions and their effects on ecological issues, particle transport, sediment re-suspension, and erosion in stratified lakes is a worthwhile future endeavor.

Acknowledgements

Reference

Anderson, E.J., Schwab, D.J., 2013. Predicting the oscillating bi-directional exchange flow in the Straits of Mackinac. J. Great Lakes Res. 39 (4), 663–671.

Bardou, M., Birk, K., 2012. Twenty-Three Foot Waves on Lake Michigan! Examining Storm Events on the Lake. National Weather Service, Chicago. [www.crh.noaa.gov].

Battjes, J.A., Janssen, J.P.F.M., 1978. Energy loss and set-up due to breaking of random waves. In: Coastal Engineering Proceedings. Am. Soc. Civ. Eng., N.Y., pp. 569–588.

Beardsley, R.C., Chen, C., Xu, Q., 2013. Coastal flooding in Scituate (MA): a FVCOM study of the 27 December 2010 nor'easter. J. Geophys. Res. 118 (11), 6030–6045.

Beletsky, D., Schwab, D.J., 2001. Modeling circulation and thermal structure in Lake Michigan: annual cycle and interannual variability. J. Geophys. Res. 106 (C9), 19745–19771.

Beletsky, D., Schwab, D.J., McCormick, M., 2006. Modeling the 1998–2003 summer circulation and thermal structure in Lake Michigan. J. Geophys. Res. 11, C10010. doi:10.1029/2005JC003222.

Beletsky, D., Schwab, D.J., Roebber, P.J., McCormick, M.J., Miller, G.S., Saylor, J.H., 2003. Modeling wind-driven circulation during the March 1998 sediment resuspension event in Lake Michigan. J. Geophys. Res. 108, 3038. doi:10.1029/2001JC001159, C2.

Benetazzo, A., Carniel, S., Sclavo, M., Bergamasco, A., 2013. Wave–current interaction: effect on the wave field in a semi-enclosed basin. Ocean Modell 70, 152–165.

Booij, N., Ris, R.C., Holthuijsen, L.H., 1999. A third-generation wave model for coastal regions: 1. Model description and validation. J. Geophys. Res. 104 (C4), 7649–7666.

Bolaños, R., Sørensen, J.V.T., Benetazzo, A., Carniel, S., Sclavo, M., 2014. Modelling ocean currents in the northern Adriatic Sea. Cont. Shelf Res. 87, 54–72.

Bunya, S., Dietrich, J.C., Westerink, J.J., Ebersole, B.A., Smith, J.M., Atkinson, J.H., Roberts, H.J., 2010. A high-resolution coupled riverine flow, tide, wind, wind wave, and storm surge model for southern Louisiana and Mississippi. Part I: model development and validation. Mon. Weather Rev. 138 (2), 345–377.

Carniel, S., Warner, J.C., Chiggiato, J., Sclavo, M., 2009. Investigating the impact of surface wave breaking on modeling the trajectories of drifters in the northern Adriatic Sea during a wind-storm event. Ocean Modell 30 (2), 225–239.

Chen, C., Beardsley, R.C., Luettich, R.A., Westerink, J.J., Wang, H., Perrie, W., Toulany, B., 2013. Extratropical storm inundation testbed: intermodel comparisons in Scituate, Massachusetts. J. Geophys. Res. 118 (10), 5054–5073.

Chen, C., Liu, H., Beardsley, R.C., 2003. An unstructured grid, finite-volume, three-dimensional, primitive equations ocean model: application to coastal ocean and estuaries. J. Atmos. Ocean. Tech. 20 (1), 159–186.

Chen, C., Qi, J., Li, C., Beardsley, R.C., Lin, H., Walker, R., Gates, K., 2008. Complexity of the flooding/drying process in an estuarine tidal-creek salt-marsh system: an application of FVCOM. J. Geophys. Res. 11, C07052. doi:10.1029/2007JC004328.

Chen, C., et al., 2004. Impacts of suspended sediment on the ecosystem in Lake Michigan: a comparison between the 1998 and 1999 plume events. J. Geophys. Res. 109, C10S05. doi:10.1029/2002JC001687.

Chen, C., et al., 2011. An Unstructured Grid, Finite-Volume Coastal Ocean Model, p. 373 FVCOM User Manual. SMAST/UMASSD Tech. Rep. 11 (1101).

Chittibabu, P., Rao, Y.R., 2012. Numerical simulation of storm surges in Lake Winnipeg. Nat. Hazard. 60 (2), 181–197.

Côté, J., Gravel, S., Méthot, A., Patoine, A., Roch, M., Staniforth, A., 1998. The operational CMC-MRB global environmental multiscale (GEM) model. Part I: design considerations and formulation. Mon. Weather Rev. 126 (6), 1373–1395.

Craik, A.D., Leibovich, S., 1976. A rational model for Langmuir circulation. J. Fluid Mech. 73 (03), 401–426.

Dawson, C., Westerink, J.J., Feyen, J.C., Pothina, D., 2006. Continuous, discontinuous and coupled discontinuous–continuous Galerkin finite element methods for the shallow water equations. Int. J. Numer. Methods Fluids 52 (1), 63–88.

Dietrich, J.C., Bunya, S., Westerink, J.J., Ebersole, B.A., Smith, J.M., Atkinson, J.H., Roberts, H.J., 2010. A high-resolution coupled riverine flow, tide, wind, wind wave, and storm surge model for southern Louisiana and Mississippi. Part II: synoptic description and analysis of Hurricanes Katrina and Rita. Mon. Weather Rev. 138 (2), 378–404.

Dietrich, J.C., Tanaka, S., Westerink, J.J., Dawson, C.N., Luettich, R.A., Zijlema, M., Westerink, H.J., 2012. Performance of the unstructured-mesh, SWAN+ADCIRC model in computing hurricane waves and surge. J. Sci. Comput. 52 (2), 468–497.

Dietrich, J.C., Zijlema, M., Westerink, J.J., Holthuijsen, L.H., Dawson, C.N., Luettich, R.A., Stone, G.W., 2011. Modeling hurricane waves and storm surge using integrally-coupled, scalable computations. Coast. Eng. 58 (1), 45–65.

Dodet, G., Bertin, X., Bruneau, N., Fortunato, A.B., Nahon, A., Roland, A., 2013. Wave-current interactions in a wave-dominated tidal inlet. J. Geophys. Res. 118 (3), 1587–1605.

Donelan, M.A., Babanin, A.V., Young, I.R., Banner, M.L., 2006. Wave-follower field measurements of the wind-input spectral function. Part II: parameterization of the wind input. J. Phys. Oceanogr. 36 (8), 1672–1689.

Donelan, M.A., Dobson, F.W., Smith, S.D., Anderson, R.J., 1993. On the dependence of sea surface roughness on wave development. J. Phys. Oceanogr. 23, 2143–2149.

Fairall, C.W., Bradley, E.F., Rogers, D.P., Edson, J.B., Young, G.S., 1996. Bulk parameterization of air-sea fluxes for Tropical Ocean-Global Atmosphere Coupled-Ocean Atmosphere Response Experiment. J. Geophys. Res. 101 (C2), 3747–3764.

Galperin, B., Kantha, L.H., Hassid, S., Rosati, A., 1988. A quasi-equilibrium turbulent energy model for geophysical flows. J. Atmos. Sci. 45 (1), 55–62.

Garratt, J.R., 1977. Review of drag coefficients over oceans and continents. Mon. Weather Rev. 105 (7), 915–929.

He, R., Liu, Y., Weisberg, R.H., 2004. Coastal ocean wind fields gauged against the performance of an ocean circulation model. Geophys. Res. Lett. 31, L14303. doi:10.1029/2003GL019261.

Hesser, T.J., Cialone, M.A., Anderson, M.E., 2013. Lake St. Clair: Storm Wave and Water Level Modeling. U.S. Army Eng. Res. and Dev. Cent. Coastal and Hydraul. Lab., Vicksberg, Miss Rep. ERDC/CHL-TR-13-5.

Holthuijsen, L.H., 2007. Waves in Oceanic and Coastal Waters. Cambridge University Press.

Hopkins, J., Elgar, S., Raubenheimer, B., 2016. Observations and model simulations of wave-current interaction on the inner shelf. J. Geophys. Res. 121 (1), 198–208.

Janssen, P.A., 1991. Quasi-linear theory of wind-wave generation applied to wave forecasting. J. Phys. Oceanogr. 21 (11), 1631–1642.

Jensen, R.E., Cialone, M.A., Chapman, R.S., Ebersole, B.A., Anderson, M., Thomas, L., 2012. Lake Michigan Storm: Wave and Water Level Modeling. U.S. Army Eng. Res. and Dev. Cent. Coastal and Hydraul. Lab., Vicksberg, Miss Rep. ERDC/CHL-TR-12-26.

Kerr, P.C., Martyr, R.C., Donahue, A.S., Hope, M.E., Westerink, J.J., Luettich, R.A., Westerink, H.J., 2013a. US IOOS coastal and ocean modeling testbed: evaluation of tide, wave, and hurricane surge response sensitivities to mesh resolution and friction in the Gulf of Mexico. J. Geophys. Res. 118 (9), 4633–4661.

Kerr, P.C., Donahue, A.S., Westerink, J.J., Luettich, R.A., Zheng, L.Y., Weisberg, R.H., Cox, A.T., 2013b. US IOOS coastal and ocean modeling testbed: inter-model evaluation of tides, waves, and hurricane surge in the Gulf of Mexico. J. Geophys. Res. 118 (10), 5129–5172.

Kim, S.Y., Yasuda, T., Mase, H., 2010. Wave set-up in the storm surge along open coasts during Typhoon Anita. Coast. Eng. 57 (7), 631–642.

Kirby, J.T., Chen, T.-M., 1989. Surface waves on vertically sheared flows: approximate dispersion relations. J. Geophys. Res. 94 (C1), 1013–1027.

Komen, G.J., Hasselmann, S., Hasselmann, K., 1984. On the existence of a fully developed wind-sea spectrum. J. Phys. Oceanogr. 14 (8), 1271–1285.

Kumar, N., Voulgaris, G., Warner, J.C., Olabarrieta, M., 2012. Implementation of the vortex force formalism in the coupled ocean-atmosphere-wave-sediment transport (COAWST) modeling system for inner shelf and surf zone applications. Ocean Modell 47, 65–95.

Lane, E.M., Restrepo, J.M., McWilliams, J.C., 2007. Wave–current interaction: a comparison of radiation-stress and vortex-force representations. J. Phys. Oceanogr. 37 (5), 1122–1141.

Lang, G.A., Leshkevich, G.A., 2014. Persistent wind fields over the Great Lakes, 2002–2013. In: Paper presented at 57th Annual Conference on Great Lakes Research. McMaster Univ., Hamilton, Ontario, Canada, pp. 26–30. May.

Large, W.G., Pond, S., 1981. Open ocean momentum flux measurements in moderate to strong winds. J. Phys. Oceanogr. 11 (3), 324–336.

Liu, H., Xie, L., 2009. A numerical study on the effects of wave–current–surge interactions on the height and propagation of sea surface waves in Charleston Harbor during Hurricane Hugo 1989. Cont. Shelf Res. 29 (11), 1454–1463.

Longuet-Higgins, M.S., Stewart, R.W., 1964. Radiation stresses in water waves; a physical discussion, with applications. Deep Sea Res. Oceanogr. Abstr. 11 (4), 529–562.

Luettich, R.A., Westerink, J.J., 2004. Formulation and Numerical Implementation of the 2D/3D ADCIRC Finite Element Model Version 44.XX, p. 74 Available from: [http://www.unc.edu/ims/adcirc/adcirc_theory_2004_12_08.pdf].

Madsen, O.S., 1994. Spectral wave-current bottom boundary layer flows. In: Edge, B.L. (Ed.), Proc. 21st Conf. Coastal Eng.. Am. Soc. of Civ. Eng., Reston, VA, pp. 623–634.

Mao, M., van der Westhuysen, A.J., Xia, M., Schwab, D.J., Chawla, A., 2016. Modeling wind waves from deep to shallow waters in Lake Michigan using unstructured SWAN. J. Geophys. Res. 121, 3836–3865. doi:10.1002/2015JC011340.

McCombs, M.P., Mulligan, R.P., Boegman, L., Rao, Y.R., 2014. Modeling surface waves and wind-driven circulation in eastern Lake Ontario during winter storms. J. Great Lakes Res. 40, 130–142.

McWilliams, J.C., Restrepo, J.M., Lane, E.M., 2004. An asymptotic theory for the interaction of waves and currents in coastal waters. J. Fluid Mech. 511, 135–178.

Mellor, G.L., 2008. The depth-dependent current and wave interaction equations: a revision. J. Phys. Oceanogr. 38 (11), 2587–2596.

Mellor, G.L., Blumberg, A., 2004. Wave breaking and ocean surface layer thermal response. J. Phys. Oceanogr. 34 (3), 693–698.

Mellor, G.L., Ezer, T., Oey, L.-Y., 1994. The pressure gradient conundrum of sigma coordinate ocean models. J. Atmos. Ocean. Tech. 11 (4), 1126–1134.

Mellor, G.L., Oey, L.-Y., Ezer, T., 1998. Sigma coordinate pressure gradient errors and the seamount problem. J. Atmos. Ocean. Tech. 15 (5), 1122–1131.

Mellor, G.L., Yamada, T., 1982. Development of a turbulence closure model for geophysical fluid problems. Rev. Geophys. 20 (4), 851–875.

Niu, Q., Xia, M., Rutherford, E.S., Mason, D.M., Anderson, E.J., Schwab, D.J., 2015. Investigation of interbasin exchange and interannual variability in Lake Erie using an unstructured-grid hydrodynamic model. J. Geophys. Res. 120 (3), 2212–2232.

Olabarrieta, M., Warner, J.C., Kumar, N., 2011. Wave–current interaction in Willapa Bay. J. Geophys. Res. 116, C2014. doi:10.1029/2011JC007387.

Osuna, P., Monbaliu, J., 2004. Wave–current interaction in the Southern North Sea. J. Marine Syst. 52 (1), 65–87.

O'Connor, W.P., Schwab, D.J., Lang, G.A., 1999. Forecast verification for Eta Model winds using Lake Erie storm surge water levels. Weather Forecast 14 (1), 119–133.

Phillips, O.M., 1977. The Dynamics of the Upper Ocean. Cambridge University Press.

Pullen, J., Doyle, J.D., Haack, T., Dorman, C., Signell, R.P., Lee, C.M., 2007. Bora event variability and the role of air-sea feedback. J. Geophys. Res. 112, C03S18. doi:10.1029/2006JC003726.

Powell, M.D., Vickery, P.J., Reinhold, T.A., 2003. Reduced drag coefficient for high wind speeds in tropical cyclones. Nature 422 (6929), 279–283.

Qi, J., Chen, C., Beardsley, R.C., Perrie, W., Cowles, G.W., Lai, Z., 2009. An unstructured-grid finite-volume surface wave model (FVCOM-SWAVE): implementation, validations and applications. Ocean Modell 28 (1), 153–166.

Rogers, W.E., Hwang, P.A., Wang, D.W., 2003. Investigation of Wave Growth and decay in the SWAN model: three Regional-Scale applications. J. Phys. Oceanogr. 33 (2), 366–389.

Roland, A., Cucco, A., Ferrarin, C., Hsu, T.-W., Liau, J.-M., Ou, S.-H., Umgiesser, G., Zanke, U., 2009. On the development and verification of a 2-D coupled wave-current model on unstructured meshes. J. Marine Syst. 78, S244–S254.

Röhrs, J, Christensen, K.H., Hole, L.R., Broström, G., Drivdal, M., Sundby, S., 2012. Observation-based evaluation of surface wave effects on currents and trajectory forecasts. Ocean Dyn. 62, 1519–1533.

Saha, S., et al., 2014. The NCEP climate forecast system version 2. J. Clim. 27 (6), 2185–2208.

Schwab, D.J., Morton, J.A., 1984. Estimation of overlake wind speed from overland wind speed: a comparison of three methods. J. Great Lakes Res. 10 (1), 68–72.

Schwab, D.J., Beletsky, D., Lou, J., 2000. The 1998 coastal turbidity plume in Lake Michigan. Estuar. Coastal Shelf Sci. 50 (1), 49–58.

Sheng, Y.P., Liu, T., 2011. Three-dimensional simulation of wave-induced circulation: comparison of three radiation stress formulations. J. Geophys. Res. 116, C05021. doi:10.1029/2010JC006765.

Smagorinsky, J., 1963. General circulation experiments with the primitive equations: I. the basic experiment. Mon. Weather Rev. 91 (3), 99–164.

Snyder, R.L., Dobson, F.W., Elliott, J.A., Long, R.B., 1981. Array measurements of atmospheric pressure fluctuations above surface gravity waves. J. Fluid Mech. 102, 1–59.

Sun, Y., Chen, C., Beardsley, R.C., Xu, Q., Qi, J., Lin, L., 2013. Impact of current–wave interaction on storm surge simulation: a case study for Hurricane Bob. J. Geophys. Res. 118 (5), 2685–2701.

SWAN Group, 2012a. SWAN Scientific and Technical Documentation—SWAN Cycle III version 40.91. Delft Univ. of Technol., Delft, Netherlands, pp. 43–51. chap. 3[Available at http://www.swan.tudelft.nl].

SWAN Group, 2012b. SWAN User Manual-SWAN Cycle III Version 40.91. Delft Univ. of Technol., Delft, Netherlands, pp. 55–56. chap. 4[Available at http://www.swan.tudelft.nl].

Swineford, J.T., DeVries, J.K., DeVries, N., Gorter, J.D., Santucci, J., Spykman, J.T., 2014. The impacts of three autumn storms on a Lake Michigan foredune. J. Clim. 11, 61–71.

Thornton, E.B., Guza, R.T., 1983. Transformation of wave height distribution. J. Geophys. Res. 88 (10), 5925–5938.

Warner, J.C., Armstrong, B., He, R., Zambon, J.B., 2010. Development of a coupled ocean–atmosphere–wave–sediment transport (COAWST) modeling system. Ocean Modell. 35 (3), 230–244.

Weisberg, R.H., Zheng, L., 2008. Hurricane storm surge simulations comparing three-dimensional with two-dimensional formulations based on an Ivan-like storm over the Tampa Bay, Florida region. J. Geophys. Res. 113, C12001. doi:10.1029/2008JC005115.

Wolf, J., Prandle, D., 1999. Some observations of wave–current interaction. Coast. Eng. 37 (3), 471–485.

Wu, L., Chen, C., Guo, P., Shi, M., Qi, J., Ge, J., 2011. A FVCOM-based unstructured grid wave, current, sediment transport model, I. Model description and validation. J. Ocean Univ. China 10 (1), 1–8.

Xie, L., Liu, H., Peng, M., 2008. The effect of wave–current interactions on the storm surge and inundation in Charleston Harbor during Hurricane Hugo 1989. Ocean Modell 20 (3), 252–269.

Zijlema, M., 2010. Computation of wind-wave spectra in coastal waters with SWAN on unstructured grids. Coast. Eng. 57 (3), 267–277.